

Article

Optimal Tuning of Fractional Order Controllers for Dual Active Bridge-Based DC Microgrid Including Voltage Stability Assessment

Mohamed Azab^{1,2,*}  and Alexandre Serrano-Fontova³ ¹ Electrical Engineering Technology Department, Faculty of Engineering, Benha University, Benha 13512, Egypt² Electrical Engineering Technology Department, Yanbu Industrial College, Yanbu 30436, Saudi Arabia³ Department of Electrical Engineering, Technical University of Catalunya (UPC), 08028 Barcelona, Spain; alexandre.serrano@upc.edu

* Correspondence: mohamed.ahmed.azab@ieee.org

Abstract: In this article, three evolutionary search algorithms: particle swarm optimization (PSO), simulated annealing (SA) and genetic algorithms (GA), have been employed to determine the optimal parameter values of the fractional-order (FO)-PI controllers implemented in the dual active bridge-based (DAB) DC microgrid. The optimum strategy to obtain the parameters of these FO-PI controllers is still a major challenge for many power systems applications. The FO-PI controllers implemented in the DAB are used to control the DC link voltage to the desired value and limit the current flowing through the converter. Accordingly, the investigated control system has six parameters to be tuned simultaneously; K_{p1} , K_{i1} , λ_1 for FO-PI voltage controller and K_{p2} , K_{i2} , λ_2 for FO-PI current controller. Crucially, this tuning optimization process has been developed to enhance the voltage stability of a DC microgrid. By observing the frequency-domain analysis of the closed-loop and the results of the subsequent time-domain simulations, it has been demonstrated that the evolutionary algorithms have provided optimal controller gains, which ensures the voltage stability of the DC microgrid. The main contribution of the article can be considered in the successful application of evolutionary search algorithms to tune the parameters of FO-based dual loop controllers of a DC microgrid scheme whose power conditioner is a DAB topology.

Keywords: DAB converter; microgrid; fractional order controller; genetic algorithms; simulated annealing; particle swarm optimization; voltage stability



Citation: Azab, M.; Serrano-Fontova, A. Optimal Tuning of Fractional Order Controllers for Dual Active Bridge-Based DC Microgrid Including Voltage Stability Assessment. *Electronics* **2021**, *10*, 1109. <https://doi.org/10.3390/electronics10091109>

Academic Editors: Mehdi Narimani and Apparao Dekka

Received: 19 March 2021

Accepted: 1 May 2021

Published: 8 May 2021

Publisher's Note: MDPI stays neutral with regard to jurisdictional claims in published maps and institutional affiliations.



Copyright: © 2021 by the authors. Licensee MDPI, Basel, Switzerland. This article is an open access article distributed under the terms and conditions of the Creative Commons Attribution (CC BY) license (<https://creativecommons.org/licenses/by/4.0/>).

1. Introduction

The dual active bridge (DAB) converter is considered as one of the most critical emerging topologies that have been successfully used in many electrical power applications such as DC microgrids [1,2]. The DAB offers key advantages such as a minimum size of passive filter components and high-power density when compared with other bidirectional DC-DC converters [3]. Therefore, DAB converter has gained popularity during the last decade in applications such as electric vehicles (EVs), energy management systems or DC microgrids with energy storage systems (ESS) [4–8].

A general average model of a DAB has been proposed in [2], whereas a simple but reliable model has been proposed in [7]. In Reference [7], the DAB converter average and small-signal models have been validated through both simulations and experimental tests for the four different control modes. The DABs have also been the object of study in [9–20]. Even though several control strategies have been explored for the DAB, the most common among practitioners is the simple phase shift modulation technique [17,18] based on conventional PI controllers [20,21]. Besides, the variable structure controllers have been employed to control the DAB's operation, as can be seen in [22].

Given the proliferation of the DC and mixed AC/DC microgrids, some research has been carried out to evaluate the capabilities of some power electronic converters for

voltage stability. In this sense, the voltage droop has been one of the most commonly adopted voltage regulation solutions in these microgrids. However, some articles have proposed modified versions of this classical voltage droop, see [23–25]. In particular, in [23], a disturbance observer has been designed for voltage regulation. In Reference [24], a damping controller has been designed to avoid power oscillations. Reference [25] proposed an observer-based with both voltage droop and current feedforward control in a DC microgrid.

On the other hand, voltage stability has also gained scientific researchers' attention, see [26–29]. In fact, power oscillations are a consequence of poorly damped scenarios. Thus, some of them have investigated the DC microgrids' stability, considering the passivity-based criterion [26,27]. The power converters impedance modelling for voltage stability in DC microgrids is explored in [28]. In Reference [29], a stability preserving criterion has been designed for DC microgrids considering a floating bus. The stability assessment with controller optimization has been analyzed in [30]. Lastly, an in-depth review of the available strategies used for voltage stability in DC systems is detailed in [31].

Microgrid controllers are used for either stabilization or regulation and are commonly based on feedforward cascaded loops with PI regulators. Nonetheless, the so-called fractional-order PI controllers (FO-PI) exhibit better characteristics compared with conventional PI ones [32–35]. Therefore, in this article, the FO-PI controllers have been utilized instead of conventional PI controllers. Owing to the existence of multiple FO controller parameters to be tuned simultaneously, evolutionary search algorithms have been employed to determine those controllers' optimum value.

As stated above, several relevant works have been carried out for the voltage stability in DC microgrids. However, even though these works have made significant contributions with successful results in the field, the implemented controller parameters have been considered a fixed input.

This paper presents an optimal strategy to tune the FO-PI controllers implemented in the DAB-based DC microgrid. The tuning process has been carried out with a multiobjective optimization problem formulated through three different evolutionary algorithms named GA, PSO and SA. The process to achieve the optimal controller parameters for voltage stability is described below.

The first step is to obtain the three sets of controller parameters for each algorithm. For that purpose, the whole closed-loop transfer function is implemented in Matlab/Simulink, where the small-signal stability model of the DAB is considered. After that, each evolutionary algorithm is executed. Once the convergence has been achieved in the optimization processes, each algorithm's best controller parameters are obtained.

Secondly, taking advantage of previously obtained controller parameters for each algorithm, the stability evaluation is explored. The passivity-based criterion is used to predict the stability of the implemented feedforward cascaded loop, see [36]. Thence, the frequency-domain analysis of both the open-loop controllers (i.e., inner and outer loops) and the whole closed-loop is presented.

Thirdly, in order to verify the predicted stability, the detailed model of the DC microgrid system has been implemented in PSIM, where the time-domain simulations have been performed.

The rest of the paper is organized as follows: Section 2 provides a literature review of the main control strategies used for the DAB converter. Section 3 presents a brief comparison between conventional PI and FO-PI controllers. In Section 4, the model implemented for each component of the DC microgrid is illustrated. The flowcharts and the data of each multi-objective algorithm used in the tuning process are displayed in Section 5. Section 6 explores and evaluates the stability features of the microgrid controllers through frequency-domain analysis. Afterwards, Section 7 exhibits the time-domain simulations results for several test cases and discusses the accuracy of the adopted model. Section 8 provides an in-depth comparison with other recently published articles to highlight the

contribution of the proposed methodology. Finally, the main conclusions of the paper are summarized in Section 9.

2. Literature Review

Several research activities have been focused on the control techniques of the DAB during the past few years, see [1–13]. A comprehensive overview of different modulation strategies of DAB converters is presented in [1]. In Reference [2], an HFT DAB topology including an efficiency optimization-based modulation strategy is proposed. In Reference [3], state-feedback techniques and linear matrix inequalities technique have been employed to control DAB converter operation. The proposed approach provides a fast transient response and improves the robustness against load and voltage variations. A hybrid modulation strategy for DAB converter that improves the efficiency over a wide range of input voltage and load variations has been proposed in [4,5]. In Reference [6], a per-unit model of DAB converter has been developed, where the article also addressed an optimized control technique based on the triple-phase shift (TPS) technique. The authors of [7] proposed a simple phase-shift modulation technique based on the parabolic carrier concept that has been implemented digitally through Verilog and hardware digital circuits. Investigators in [8,9] suggested several modulation methods for the DAB converter to avoid transformer saturation.

In References [10,11], a model predictive control (MPC) approach has been employed to control the operation of DAB converter. While in [12,13] the DAB control scheme is based on direct power control concept. In References [14–16], the current modulation schemes enhance the transient response of the DAB and reduce the low order harmonics in the current waveform. A bi-directional power flow scheme has been proposed in [17], where the power flow between the AC main grid and DC microgrid is controlled through a DAB converter. In References [18,19], the reactive power control of a DAB converter is assessed. Reference [20] focused on reducing the current stress. While a power flow scheme has been proposed in [21] to control the power transfer between two microgrids.

Many efforts have been carried out to improve DAB converter performance for many purposes. In this vein, the authors of [37–40] have achieved considerable DAB converter modelling improvements.

2.1. Application of FO-PI Controllers

Indeed, the FO controllers have gained interest in recent years [41–50]. In Reference [41], a survey of state-of-the-art advances in FO control specifically for time-delay systems provided. In Reference [42], a detailed design and tuning of robust FO controller employed for autonomous microgrid system are presented. In Reference [43], FPGA has been utilized to implement the FO controllers, while the authors of [44] utilized DSP to implement the FO controller. Investigators of [45] presented a tuning method and a robustness analysis of a FO controller.

Similarly, the optimal design of an FO controller to tune a pneumatic servo system has been studied in [46]. In References [47,48], the FO controllers have been utilized for closed-loop control of permanent magnet synchronous motor drives. In Reference [49], a design procedure and experimental validation of a FO controller have been used to control hydraulically powered actuator operation. The FO controllers have been employed in [50] to control the back-to-back operation of some power converters.

2.2. Tuning of FO-PI Controllers

When the parameters of fractional-order PI controllers are optimally selected, the overall control system exhibits better dynamic and steady-state performance when compared with the traditional PI controllers, see [46,47]. However, two extra parameters (i.e., the integrator and differentiator orders) result in a more complicated tuning procedure. Thence, tuning of the fractional-order PI controller parameters is still of interest, see [51–54]. In Reference [51], the tuning of an FO-PI controller has been carried out using a genetic algorithm.

On the other hand, [52] proposed and derived unified fractional complex order controller expressions as a universal structure. Reference [53] presented an atom search optimization algorithm and its chaotic version to determine the optimal parameters of the FO controller. In Reference [54], hybrid PSO optimization and grey wolf optimization methods to tune FO controller parameters are used.

In general, evolutionary search algorithms such as simulated annealing [55,56], genetic algorithms [57–60], ant colony [61–63], particle swarm optimization [64–68] and biogeography-based optimization [69] can be employed to search for the optimum values of FO controller parameters by formulating a multi-variable optimization problem.

3. Comparison between FO and Conventional PID Controllers

3.1. Conventional PID Controllers

The standard form of a conventional PID controller is expressed as Equation (1a) and represented in Figure 1, where a generalized block diagram of a single-input single-output closed-loop control system is illustrated. As is widely known, the PI controller is obtained by removing the derivative part in Equation (1a):

$$u(t) = K_p e(t) + k_i \int_0^t e(t) dt + K_d \frac{d}{dt} e(t) \quad (1a)$$

$$e(t) = y_r(t) - y(t) \quad (1b)$$

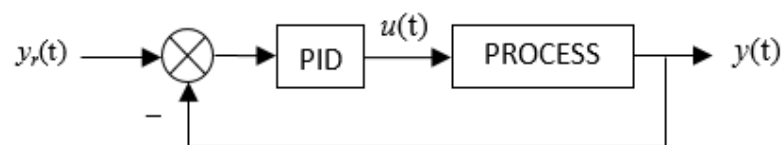


Figure 1. Block diagram of a closed loop control system with PID controller.

Accordingly, the transfer function of the conventional PID controller is described by:

$$G_{pid}(S) = K_p + \frac{K_i}{S} + K_d S \quad (2)$$

where K_p is the proportional gain, K_i is the integrator gain, K_d is the differentiator gain, $e(t)$ is the system error, and $u(t)$ is the controller output. The PID controller is still one of the preferable and commonly used controllers in many industrial applications [46,49]. Recently, FO controllers have been introduced to overcome the major drawbacks of the conventional PID controllers [41,45,46,49].

3.2. FO PID Controllers

Equation (3) describes the transfer function of a FO order PID controller:

$$G_{foc}(S) = K_p + \frac{K_i}{S^\lambda} + K_d S^\mu \quad (3)$$

where λ and μ are the order and differential terms, respectively. Compared with conventional integer-order PID controller, FO controller has integral and differential order different than unity such that (λ and $\mu \neq 1$). In fact, FO controller can be considered as a generalized form of conventional integer-order PID controller, where the conventional PID controller is achieved by setting λ and μ to unity. Other controller functions (i.e., special cases such as P, PI or PD controllers) can be obtained by assigning λ and μ to suitable values as illustrated in Figure 2, where four distinct values are indicated through the (λ - μ) plane. In several research articles, it has been reported that FO controllers provide better response time and reduce the overshoot compared with the conventional PID controllers, see for instance [42] and [47]. However, the tuning process of an FO-PID controller is far

more complex because there are many parameters to be optimized simultaneously (i.e., K_p , K_i , K_d , λ and μ). In this paper, the derivative part is removed, and therefore the two controllers are FO-PI.

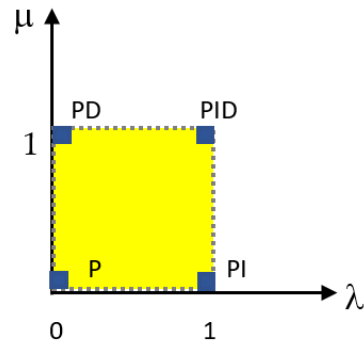


Figure 2. $(\lambda-\mu)$ plane of fractional order PID controller.

4. Test System

4.1. Block Diagram

The block diagram of the investigated system is illustrated in Figure 3, where the DC microgrid is connected to the DAB output terminal. The voltage at the DAB output terminals is used as input for the DAB voltage regulation. The DAB converter is connected to the grid through a 3-phase six-pulse uncontrolled diode rectifier. The DC bus of the microgrid is loaded with both constant impedance and constant power load models. The control unit of the DAB converter is based on a cascaded loop with the implemented FO-PI controllers. Those parameters are tuned in an offline process by the abovementioned evolutionary search algorithms; see the procedure in Section 5.

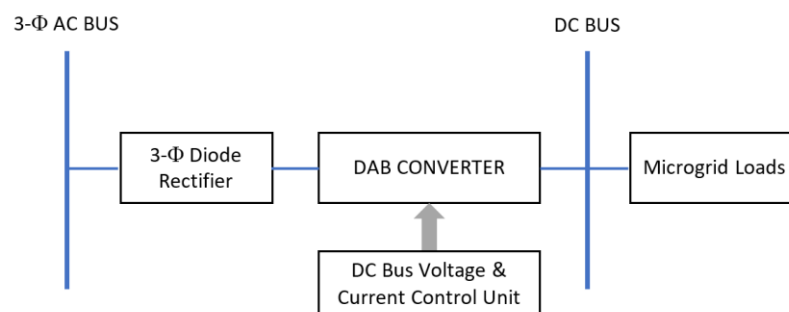


Figure 3. Block diagram of the test system.

4.2. Detailed Test System

The detailed model of the DC microgrid object of study is shown in Figure 4. According to the circuit diagram depicted in Figure 4, the whole system is composed of three stages. The first stage is the three-phase uncontrolled rectifier which feeds the DC voltage link. The second stage comprises a single-phase bridge AC/DC inverter whose output feeds the HFT transformer. In third place, the second single-phase bridge AC/DC rectifier feed the DC link. As stated above, the DC bus voltage control system comprises two control loops (i.e., the outer loop for the voltage and the inner loop for the current).

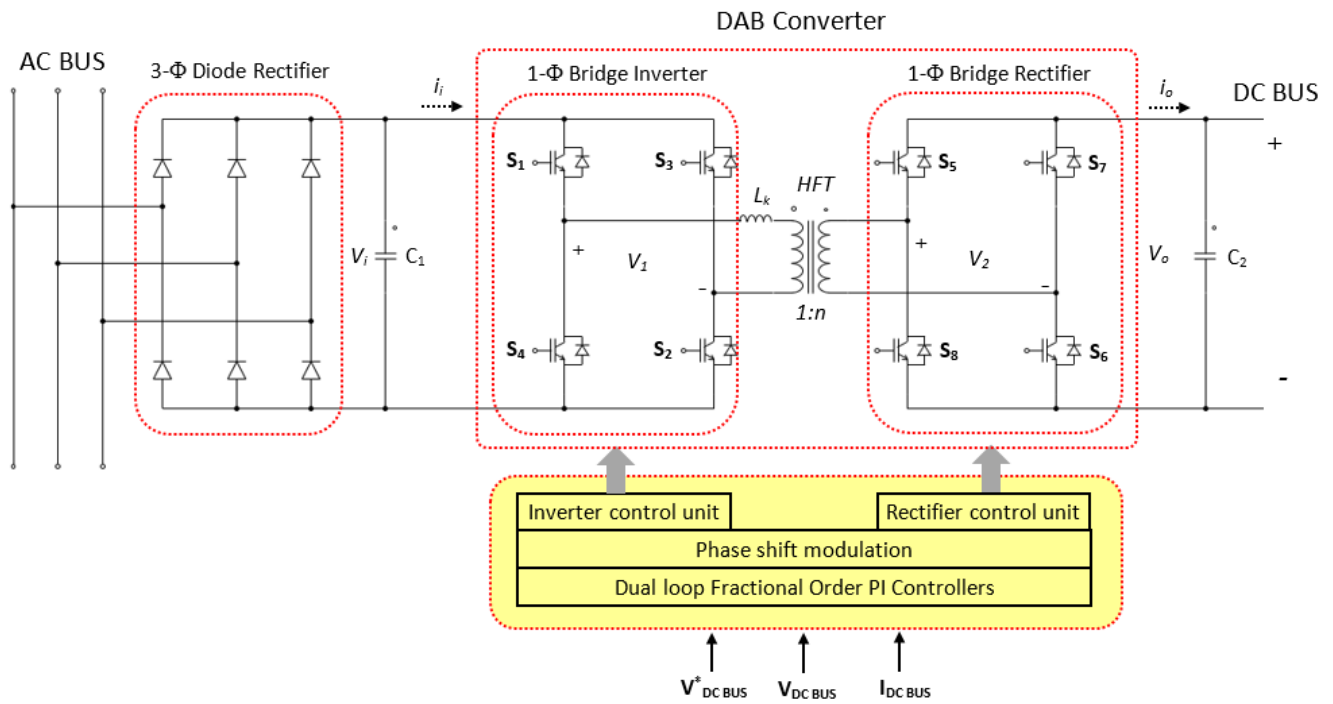


Figure 4. Circuit diagram of the investigated system.

4.3. Test System Components

This section details the model implemented in each component of the test system. The test system illustrated in Figure 4 can be divided into several elements as follows: (i) the grid and the three-phase diode rectifier, (ii) the DAB converter and (iii) the microgrid loads.

4.3.1. Main Grid and Three-Phase Rectifier

The Thevenin’s equivalent represents the impedance of the grid seen by the three-phase diode rectifier. Therefore, the AC grid is modelled through an impedance (R_{ac} and L_{ac}). A coupling impedance in the DC side of the rectifier is also added (R_{dc} and L_{dc}).

The AC voltage source and the three-phase diode rectifier can be expressed as a DC source (E_g) with an equivalent impedance (R_S and L_S) as follows [70]:

$$E_g = \frac{3\sqrt{2}}{\pi} V_g \tag{4a}$$

$$L_S = 2L_{AC} + L_{DC} \tag{4b}$$

$$R_S = 2R_{AC} + R_{DC} + \frac{3}{\pi} \omega L_{AC} \tag{4c}$$

where V_g is the line-to-line voltage of the three-phase AC system, and the last term of the equivalent series resistance in the DC side represents the effect of the commutation in the voltage drop. It is worth noting that in Figure 4, the equivalent resistance and inductance seen by the three-phase rectifier and the coupling resistance and inductance are not displayed. The data related to these parameters is provided in Appendix A.

4.3.2. Main Grid and Three-Phase Rectifier

In this subsection, the mathematical expressions of the DAB are recounted. The detailed model of a DAB has been proposed in [5]. Nevertheless, the average and small-signal models are detailed in [7]. As can be seen, the DAB is formed by two single-phase bridges with a complementary switching cycle, where two high-frequency square-wave signals are generated. The power flow regulation across the DAB can be achieved by a

shift between these two voltage signals [71–74]. These two square-wave-phase-shifted voltages create a voltage across this leakage inductance, making a current circulate through it. Thence, the current flowing through the inductor is expressed as:

$$\frac{di_{lk}}{dt} = \frac{V_1 - V_2}{L_k} \quad (5)$$

where V_1 and V_2 are the two square-wave voltages generated by the two bridges, L_k is the leakage inductance and i_{lk} the current that flows through this inductance. For each half period of the voltage signals, the relationship between voltages and currents is expressed as:

$$v_i + \frac{v_o}{n} = L_k \frac{I_1 + I_2}{dT} \quad \text{for } 0 < t < dT \quad (6a)$$

$$v_i - \frac{v_o}{n} = L_k \frac{I_1 - I_2}{(1-d)T} \quad \text{for } dT < t < T \quad (6b)$$

where I_1 and I_2 are the two currents corresponding to the leakage currents when the leading and lagging bridges are switched, n is the turns ratio of the HFT (1:n), d is the phase shift angle between the two bridge voltages, and T is half of the switching period. The switching period depends on the switching frequency f_s of the converter. Therefore Equation (6a,b) can also be computed as:

$$v_i + \frac{v_o}{n} = L_k \frac{I_1 + I_2}{d} 2f_s \quad \text{for } 0 < t < dT \quad (7a)$$

$$v_i - \frac{v_o}{n} = L_k \frac{I_1 - I_2}{(1-d)} 2f_s \quad \text{for } dT < t < T \quad (7b)$$

The average DAB output current is expressed by combining Equation (6a,b) [36]

$$\bar{i}_o = \frac{1}{nT} \left(\frac{1}{2} I_1 t_1 - \frac{1}{2} I_2 t_2 + (1-d) T I_2 + (1-d) T \frac{1}{2} (I_1 - I_2) \right) \quad (8)$$

where t_1 and t_2 are the sum of these two times are equal to the phase-shift for a half period. Terms t_1 , t_2 , I_1 and I_2 are given by:

$$I_1 = \frac{T}{2L_k} \left(2 \frac{V_o}{n} d + V_i - \frac{V_o}{n} \right) \quad (9a)$$

$$I_2 = \frac{T}{2L_k} \left(2V_i d - V_i + \frac{V_o}{n} \right) \quad (9b)$$

$$t_1 = T \left[\frac{2 \frac{V_o}{n} d + V_i - \frac{V_o}{n}}{2 \left(V_i + \frac{V_o}{n} \right)} \right] \quad (9c)$$

$$t_2 = T \left[\frac{2V_i d - V_i + \frac{V_o}{n}}{2 \left(V_i + \frac{V_o}{n} \right)} \right] \quad (9d)$$

where V_i and V_o are the DAB input and output voltages. Both the input and output average currents are represented as i_i and i_o and are computed as follows:

$$i_o = \frac{(1-d) dT V_i}{nL_k} \quad (10a)$$

$$i_i = \frac{(1-d) dT V_o}{nL_k} \quad (10b)$$

The average-model DAB converter is displayed in Figure 5, where the two current sources are represented by i_i and i_o .

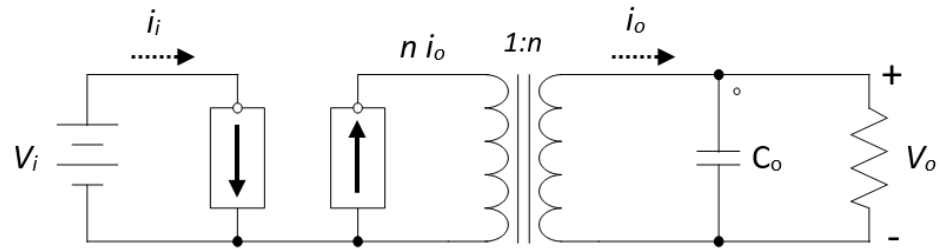


Figure 5. Averaged-model of the DAB converter.

The small-signal model is obtained by perturbing and linearizing the averaged model of Equation (10a,b) for a particular point of operation and is defined by Equation (11a,b). The small-signal model is depicted in Figure 6.

$$\hat{i}_o = C \hat{d} + B \hat{V}_i \quad (11a)$$

$$\hat{i}_i = A \hat{d} + D \hat{V}_o \quad (11b)$$

$$A = g_{id} = \frac{T(1-2D)}{nL_k} V_i \quad (11c)$$

$$B = g_{ivo} = \frac{TD(1-D)}{nL_k} \quad (11d)$$

$$C = g_{od} = \frac{T(1-2D)}{nL_k} V_o \quad (11e)$$

$$D = B = g_{ovi} = \frac{TD(1-D)}{nL_k} \quad (11f)$$

where A , B , C and D are the four current sources of the small-signal stability model observed in Figure 6, and D is the phase shift duty ratio between the square-wave signals of both bridges. These current sources are identified as g_{id} , g_{ivo} , g_{od} , g_{ovi} and expressed by Equation (11c) through Equation (11f). See the detailed procedure to obtain these values in [36]. Given Equation (11a,b), the response of the output voltage can be predicted by a first-order model as in Equation (12), where the DAB capacitance and the load resistance are expressed as unique impedance.

$$\hat{V}_o = \frac{R_o}{1 + sC_o R_o} (g_{od} \hat{d} + g_{ovi} \hat{V}_i) \quad (12)$$

where R_o and C_o are the DC microgrid load and the capacitance of the DAB output, respectively. Note that C_o is designed as C_2 in Figure 4. As shown in Equation (12), the term V_o can be affected by changes in the DAB input voltage V_i , changes in the phase-shift d , and changes in the microgrid load composition. If the microgrid load is modelled as CPL, the term R_o can be rewritten as:

$$R_o = \frac{|\hat{V}_o|^2}{P_o} \quad (13)$$

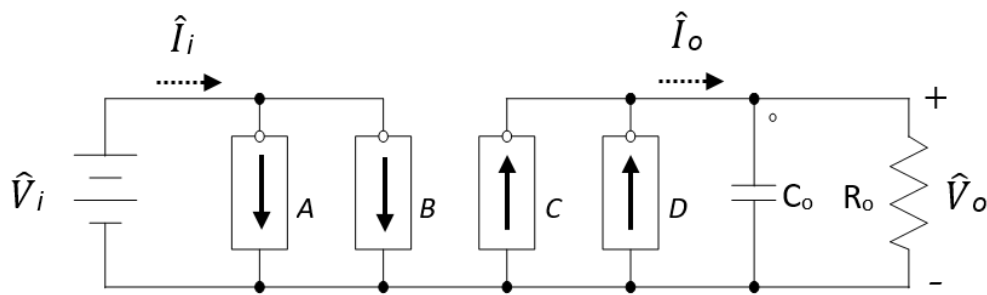


Figure 6. The small-signal model of the DAB converter.

4.4. Problem Formulation

As stated earlier, the FO controllers implemented in the DAB converter control illustrated in Figure 7 have six parameters to be tuned simultaneously. The first FO-PI controller belongs to the outer loop, which generates the current reference for the inner loop. The inner loop generates a reference for the phase-shift angle d_ϕ .

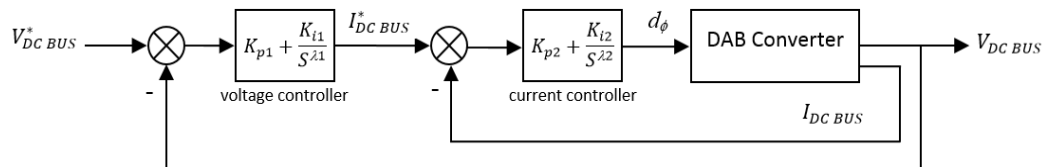


Figure 7. Dual loop control of microgrid DC bus voltage.

The three evolutionary algorithms have been used to determine the optimum values of the FO-PI controller parameter values according to the objective function described in Equation (14). This objective function has to be minimized:

$$J = |V_{DC\ BUS}^* - V_{DC\ BUS}| + |I_{DC\ BUS}^* - I_{DC\ BUS}| \tag{14}$$

5. Implemented Evolutionary Search Algorithms

5.1. Particle Swarm Optimization

The PSO algorithm is an optimization technique capable of finding globally optimal solutions using the adjacent social agent interaction. In PSO, a flock of particles flies through a search space with velocity updated by inertia movement, self-cognition, and social interaction [64]. The velocity and position of each particle is updated at each iteration by Equations (15) and (16).

$$v_i^{k+1} = w v_i^k + \alpha [L^k - x_i^k] + \beta [G^k - x_i^k] \tag{15}$$

$$x_i^{k+1} = x_i^k + v_i^{k+1} \tag{16}$$

where x_i is the position of the i -th particle in the search space, v_i is the velocity of the i -th particle, w is the inertia of particles, α and β are uniformly distributed positive random vector. L is the particle best position, G is the global best position achieved by all particles, while k is the instantaneous number of each iteration [66]. In this article, the parameters used in the PSO algorithm are presented in Table 1. The flowchart is shown in Figure 8.

Table 1. Parameters of the PSO algorithm.

Particles (Birds)	Max. Iterations	Inertia Weighting Factor w	α, β
100	100	0.05	Random number [0,1]

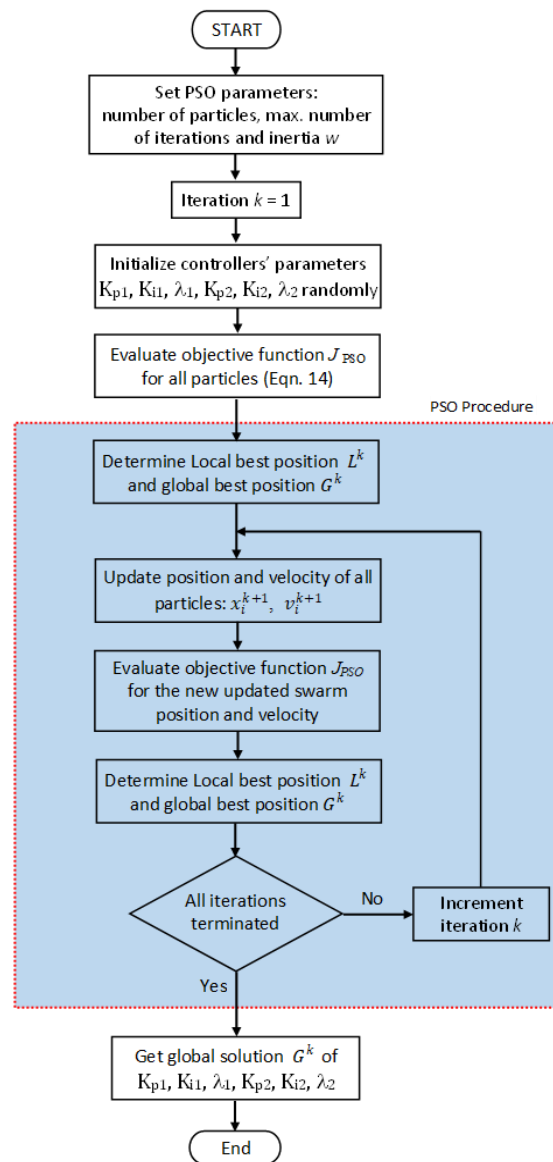


Figure 8. Flowchart implemented for the PSO algorithm.

5.2. Simulated Annealing

In the SA algorithm, the process of annealing in metals [55,56] is emulated. In the annealing process, heat is applied to a solid until it melts. Then, melted solid is allowed to cool slowly in a controlled manner. The solid reaches the minimum energy state, provided that the initial temperature is sufficiently high, and the cooling time is sufficiently long [56]. The SA algorithm requires an initial temperature, final temperature and cooling rate. An objective function is customized to represent the energy of a fictitious material. Temperature T is a control parameter, which decreases gradually as the algorithm goes further from the

initial step to the subsequent steps. The criterion of accepting a neighborhood solution n from the current solution c is given by the following probability function described by (17):

$$Prop (J_{SA}) = \left\{ \begin{array}{ll} 1 & J_{SA}(n) \leq J_{SA}(c) \\ e^{\left[\frac{J_{SA}(c)-J_{SA}(n)}{T}\right]} & J_{SA}(n) > J_{SA}(c) \end{array} \right\} \tag{17}$$

The temperature decay (decreasing) scheme in its simplest form will follow (18):

$$T_{k+1} = \alpha_1 T_k \tag{18}$$

where T_{k+1} is the temperature at step $k + 1$, T_k is the temperature at step k , and $0 \leq \alpha_1 \leq 1$. The SA parameters are detailed in Table 2 and the flowchart of this algorithm in Figure 9.

Table 2. Parameters of the SA algorithm.

Max. Iter.	Max. Function Evaluations	Initial Temp.	Annealing Parameters		
			Function	Interval	Decay Temperature
1000	$3000 \times n$	100	Boltzmann	100	Exponential

5.3. Genetic Algorithm

GA is one of the stochastic optimization search techniques that rely on natural selection. The concept of GA has been borrowed from the evolution of biology [57,58]. The process of creating the next generation from the current population toward achieving a globally optimized solution is composed of three main steps: selection, crossover and mutation. The selection rules select the individuals, called parents, that contribute to the next generation’s population, while crossover rules combine two parents to form children for the next generation [60]. The GA repeatedly modifies the population of individual solutions. At each step, the genetic algorithm selects individuals at random from the current population to be parents and uses them to produce the children for the next generation. Over successive generations, the population evolves toward an optimal solution based on the best fitted-individuals’ fitness. The parameters of the used GA for the optimal controllers optimal tuning are summarized in Table 3, whilst the flowchart is illustrated in Figure 10.

Table 3. Parameters of the GA algorithm.

PS ¹	Creation Function	Fitness Scaling	Selection	Reproduction		Mutation		Crossover Function
				Elite Count	Crossover Fraction	Function	Rate	
100	Uniform	Rank	Stochastic uniform	0.05 PS	0.8	Uniform	0.01	Scattered

¹ PS = Population size.

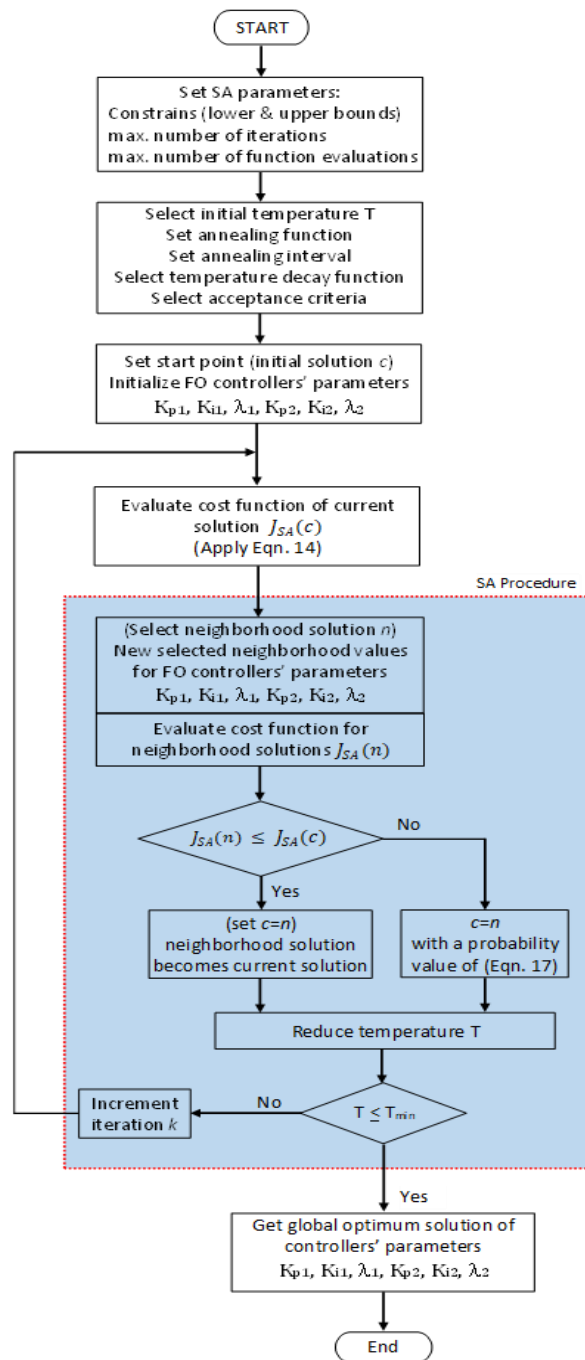


Figure 9. Flowchart implemented for the SA algorithm.

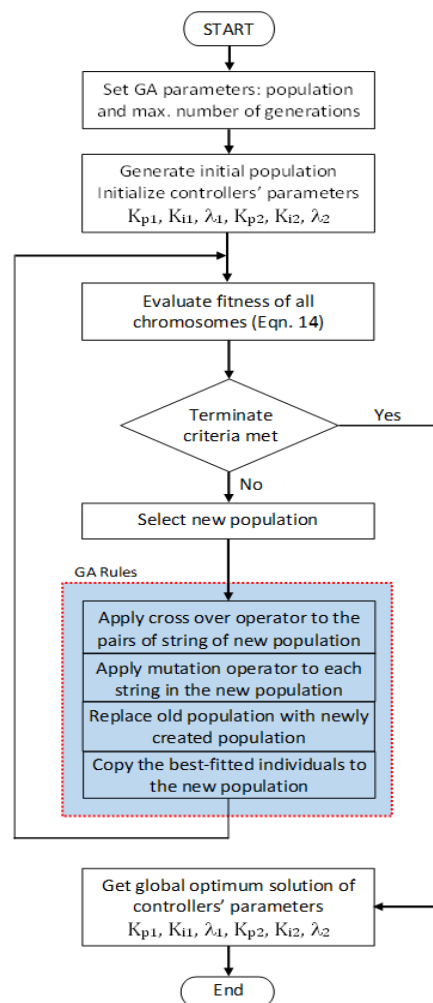


Figure 10. Flowchart implemented for the GA algorithm.

6. Stability Analysis of the DAB-Based DC Microgrid

This section evaluates the stability of the test system under investigation. For that purpose, the small-signal model of the DAB has been used. In Section 6.1, the fundamental concepts used to evaluate the stability in power converters are recalled, and the stability analysis of the microgrid object of study is provided. Finally, the results of this stability assessment are detailed and discussed in Section 6.2.

6.1. Stability Criteria and Impedance Modelling

In general, stability is assured if the ratio between (Z_{out}/Z_{in}) meets the Nyquist criterion [36]. Nevertheless, the phase of the resulting impedance Z_{out}/Z_{in} of the bode diagram must be between -90 degrees and $+90$ degrees at all frequencies. If the resulting parallel impedance phase is between -90 degrees and $+90$ degrees, the average power at the input port of the network is positive. Therefore, the system consumes energy (i.e., it is a passive system). If this impedance phase is exactly $+90$ degrees or -90 degrees, the average power is zero, and the system is lossless. If the phase is less than -90 degrees or greater than $+90$ degrees, the average power is negative, and the system injects energy (i.e., it is an active system). Therefore, the stability of a particular closed-loop system is guaranteed if the Nyquist diagram has no right half-planes (RHPs) and the contour of this diagram does not encircle the point $(-1, j\omega)$ of this plane [36].

By considering the test system shown in Figure 4, the impedance seen by the DAB input terminals is designed as Z_{out} and is represented by the grid impedance and the

equivalent coupling RLC filter (4b) and (4c). The term Z_{out} can be characterized by R_S , L_S and C_1 :

$$Z_{out} = \frac{R_S + sL_S}{s^2 C_1 L_S + s C_1 R_S + 1} \quad (19)$$

where R_S and L_S are the equivalent resistance and inductances, and C_1 is the DAB input capacitor. By linearizing and perturbing the DAB averaged model, the small-signal model can be obtained [26]. The small-signal variables are denoted by uppercase letters. As can be seen in Figure 7, the phase shift angle is obtained through the closed-loop as:

$$\hat{d} = (I_o^* - \hat{i}_o) G_C(s) \quad (20a)$$

$$I_o^* = (V_o^* - \hat{V}_o) G_V(s) \quad (20b)$$

where the subscript * denotes a reference, $G_C(s)$ and $G_V(s)$ are the inner and outer loop transfer functions, respectively. Accordingly, I_o^* is the reference value of DC bus current ($I_{DC\ BUS}^*$) previously shown in Figure 7 and given in Equation (14). Similarly, V_o^* is the reference value of DC bus voltage ($V_{DC\ BUS}^*$) previously shown in Figure 7 and given in Equation (14) as well.

By rearranging Equation (20a,b), the following expression is obtained by:

$$\hat{i}_o = \frac{(V_o^* - \hat{V}_o) G_V(s) G_C(s)}{G_C(s)} \quad (21)$$

Thus, the phase-shift \hat{d} between the square-wave voltage signals of the two bridges can be expressed as a function of (21):

$$\hat{d} = \left[\left(V_o^* - \frac{R_o \hat{i}_o}{1 + s C_2 R_o} G_V(s) \right) - \hat{i}_o \right] G_C(s) \quad (22)$$

where \hat{V}_o and \hat{i}_o are the output voltage and current of the DAB, whereas R_o is the DC load. Thereby, the voltages and currents of the DAB of the model in Figure 6, can be expressed as Equation (11a,b), where the DAB input current \hat{i}_i is as follows:

$$\hat{i}_i = \frac{T(1-2D)V_o}{nL_k} \hat{d} + \frac{TD(1-D)}{nL_k} \hat{V}_o \quad (23)$$

where V_o is the rated voltage at DAB output, n is the transformer turns ratio, L_k is the leakage inductance, and D is the phase shift duty ratio. The term T represents a half period, and f_S is the switching frequency. If the DAB input admittance C_1 is considered part of Z_{out} in (19), the closed-loop input impedance is obtained through:

$$Z_{in_CL}(s) = \frac{\hat{V}_i(s)}{\hat{i}_i(s)} \quad (24)$$

The representation of the impedance model is shown in Figure 11.

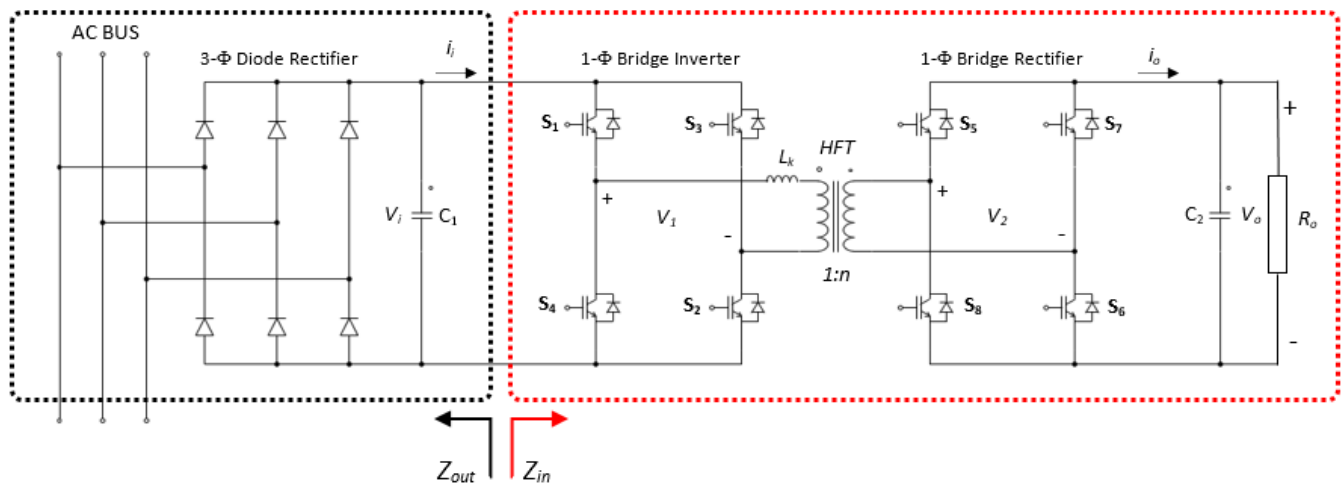


Figure 11. Impedance model.

6.2. Discussion of the Stability Analysis

In this section, the results of the frequency-domain analysis are presented. Firstly, the small-signal system stability is evaluated considering the output impedances, which is the most unfavorable scenario for stability purposes. After that, another case study is carried out considering the grid as an ideal voltage source, and as a consequence, the DAB input voltage at DAB is considered stable. Therefore, according to these two assumptions, the first considers the line and DC coupling impedances (i.e., R_{DC} , L_{DC} , R_{AC} and L_{AC}). On the contrary, the second assumes an ideal DC source voltage where these impedances are neglected.

The stability can be demonstrated by overlapping Z_{in} and the four Z_{out} impedances in the same bode plot. In Figure 12, it is seen that the input impedance of the DAB is above all these output impedances, and the phase margin is below 90 degrees. The values of these four impedances are summarized in Table 4. The larger the resistor and capacitor, the higher are the gain margin and the more stable is the system.

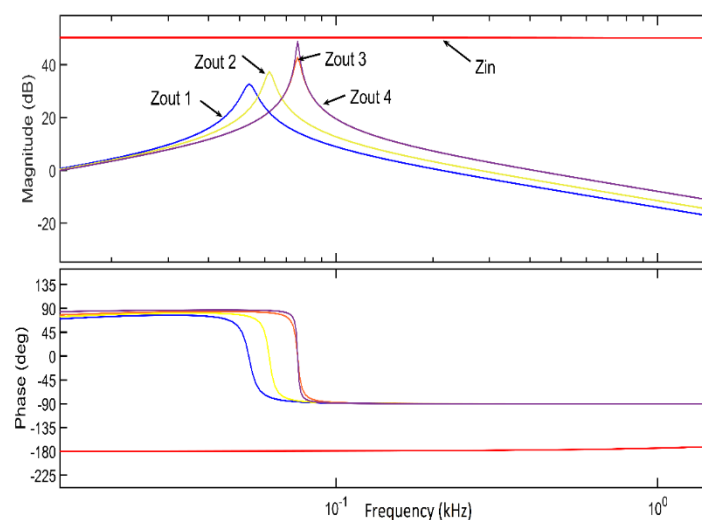
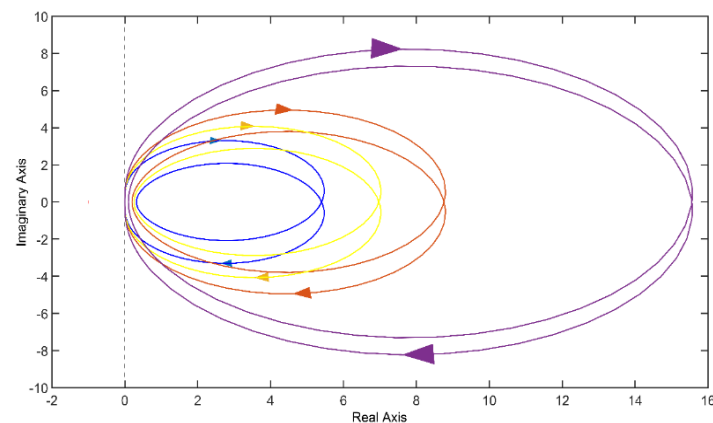


Figure 12. Bode diagram of the input and output impedances.

Table 4. Parameters of Z_{out} .

-	R (Ω)	L (H)	C (μ F)
Z_{out1}	0.32	0.011	800
Z_{out2}	0.25	0.011	600
Z_{out3}	0.2	0.011	400
Z_{out4}	0.1	0.011	400

To verify the previous explanation, the Nyquist diagram is displayed in Figure 13, where it can be seen that the four scenarios meet the stability criterion. As expected from the results in Figure 12, the most stable scenario occurs with Z_{out1} , which is the closest to the origin in Figure 13. On the contrary, the less stable case occurs when Z_{out4} is considered.

**Figure 13.** Nyquist diagram of the resulting $Z_{out} // Z_{in}$ impedances.

It is worth mentioning that the parameters in both the inner and outer loops are those obtained with the GA (i.e., $K_{p1} = 33.55$, $K_{i1} = 0.673$, $\lambda_1 = 0.217$; $K_{p2} = 4.89$; $K_{i2} = 18.24$, $\lambda_2 = 0.32$).

Once the stability of the DAB with the three-phase rectifier and the main grid has been performed, the rest of this section aims to show the performance of the parameters obtained with the three algorithms. To that purpose, as stated earlier, the main grid is now considered an ideal source and therefore, V_{in} can be regarded as stable. The Nyquist diagram of the closed-loop is illustrated in Figure 14, whereas the bode plot is shown in Figure 15. From Figure 14, it can be seen that all controllers will provide a stable response. Nevertheless, the relatively most stable results are expected when the controllers are tuned with the GA. On the contrary, the parameters obtained with the PSO algorithm may result in a relatively least robust response. The bode diagram depicted in Figure 15 is in accordance with the previous assertion. Lastly, the bode diagram of the open-loop transfer functions according to the current and voltage controllers are displayed in Figures 16 and 17, respectively.

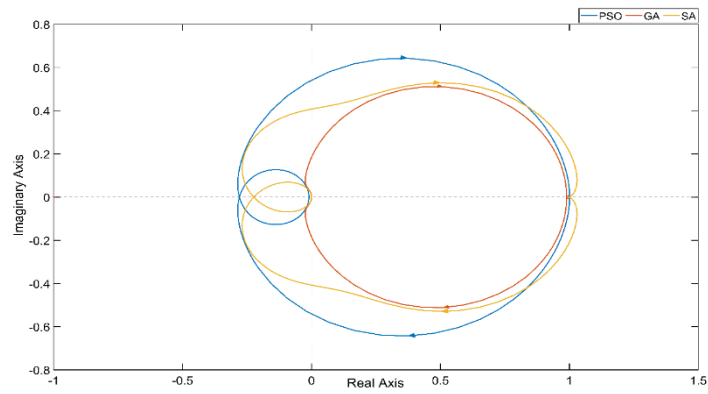


Figure 14. Nyquist diagram of the closed loop transfer function for the three evolutionary algorithms.

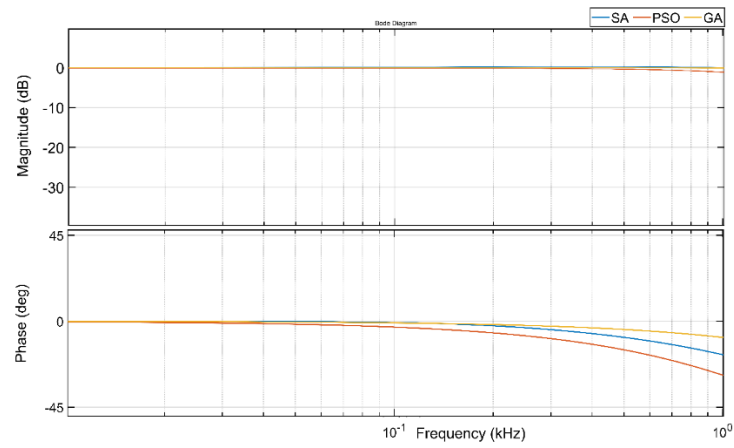


Figure 15. Bode diagram of the closed-loop transfer function for the three evolutionary algorithms.

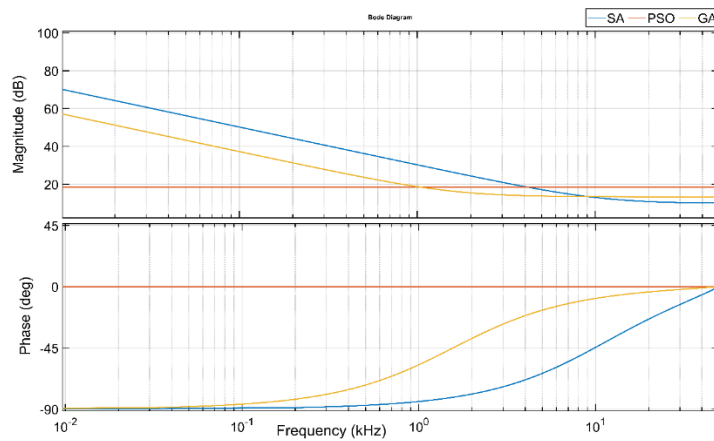


Figure 16. Bode diagram of current FO-PI controller for the three evolutionary algorithms.

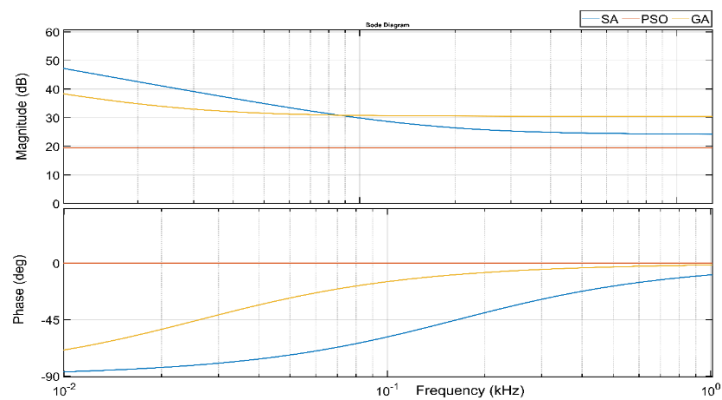


Figure 17. Bode diagram of voltage FO-PI controller for the three evolutionary algorithms.

7. Simulation Results

7.1. Simulation Parameters

Specifications and simulation parameters of the investigated system have been summarized in Appendix A in Table A1. One set of FO-PI controllers parameters obtained from each evolutionary search algorithms is summarized in Table 5. The simulation study is carried out based on these values. The overall DC microgrid system has been implemented in the PSIM software package, where the load models are displayed in Figure 18.

Table 5. Parameters of the FO-PI controller for each evolutionary algorithm.

Algorithm	Controller					
	Voltage Controller Parameters			Current Controller Parameters		
	K_{p1}	K_{i1}	λ_1	K_{p2}	K_{i2}	λ_2
PSO	9.4	0.163	1.74	8.42	0.56	1.44
SA	16.3	1	0.155	4.21	6.85	0.105
GA	33.55	0.673	0.217	4.89	18.24	0.32

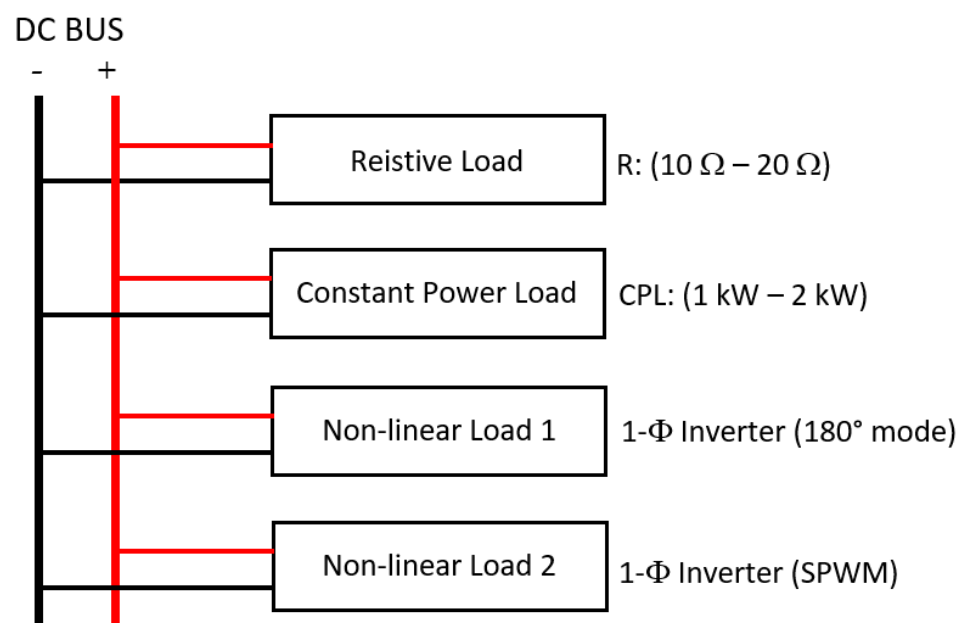


Figure 18. Different load models investigated in the DC microgrid.

7.2. Loading Conditions and Testing Scenarios

The time-domain simulations carried out with the detailed microgrid model implemented in PSIM can be divided into two major case studies. The first one tests the system's response for a step-change in the voltage reference considering a resistive load. On the other hand, the second case study analyzes a sudden load change. Within the second case study, three types of voltage-dependent load models have been considered (i.e., constant impedance, constant power, and two types of single-phase inverters feeding R and RL loads) as illustrated in Figure 18. The modelled single-phase inverters have been designed to work in two modes. The first inverter operates in square wave mode, whereas the second is a bipolar SPWM.

The responses obtained for each set of parameters obtained according to the three evolutionary algorithms are discussed and analyzed in Sections 7.3–7.5, for several load models. The optimization data is analyzed in Section 7.6, whilst a quantitative analysis of the DC microgrid performance is summarized in Table 6.

Table 6. Summary of the convergence and performance results for the three algorithms.

	ITEM	PSO	SA	GA
Algorithm convergence	Number of iterations to converge	18	40	10
	Iteration run time (s)	4–6	0.5–1	10–12
	Algorithm convergence time (min)	1.2–1.8	0.33–0.66	1.66–2
Performance under linear load (Resistive)	Settling time (s)	$\cong 0.002$	$\cong 0.002$	$\cong 0.002$
	Peak overshoot (% of reference voltage)	$\cong 3$	$\cong 3$	$\cong 3$
	Voltage ripple during load variation (%)	1.26	0.90	0.70
	Transient peak voltage dip (V)	7.5	4.5	3.75
Performance under (CPL)	Voltage dip due to sudden load change (V)	1.5	1.3	0.30
	Voltage dip due to sudden load change (%)	0.75	0.65	0.15
Performance with a single-phase inverter	Voltage dip due to sudden load change with square-wave inverter (%)	0.8	0.55	0.15
	Voltage dip due to sudden load change with SPWM inverter (%)	0.85	0.75	2.45 1.65 *
	Low-order harmonic magnitude	0.076	0.054	0.042 0.038 *
	voltage (%)			

* K_{p1} is reduced from 33.55 to 30.

7.3. System Response Considering a Resistive Load

Initially, the microgrid is loaded with a constant resistive load of 20 Ω . The voltage reference is set to 100 V, and at $t = 0.1$ s, the reference is changed to 200 V. The response of the DC bus voltage and the corresponding DC bus current are illustrated in Figures 19a, 20a and 21a according to the FO-controllers tuned by PSO, SA and GA, respectively. Based on the obtained results, the FO-PI controllers tuned by the evolutionary search algorithm result in a satisfactory transient response of the microgrid DC bus voltage.

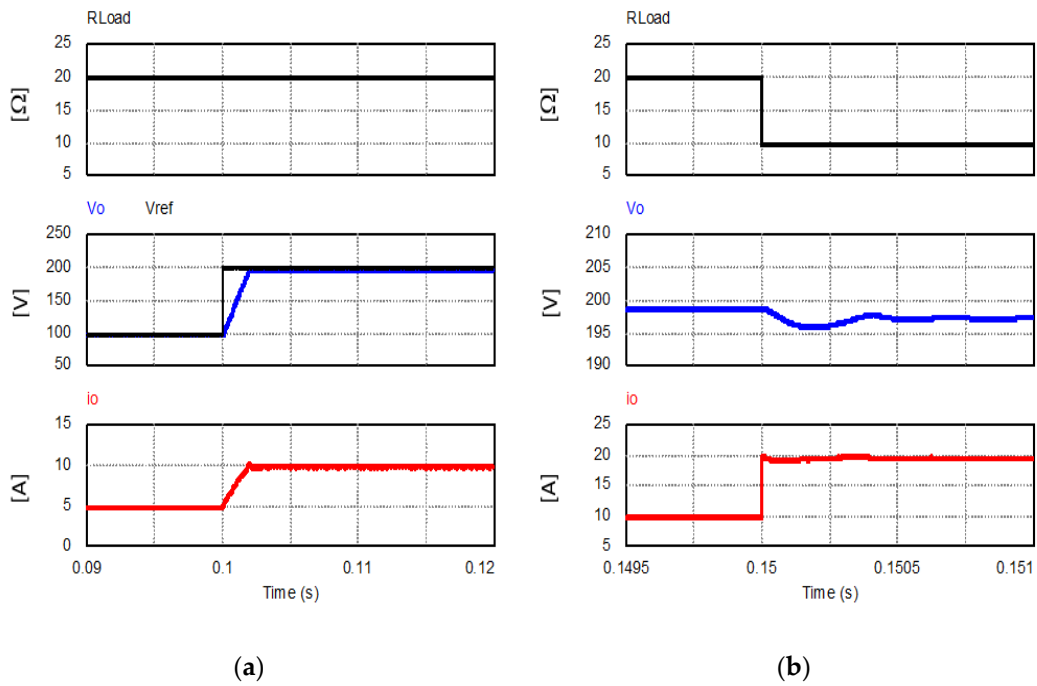


Figure 19. Simulation results with the PSO. (a) Change in voltage reference, (b) sudden load change.

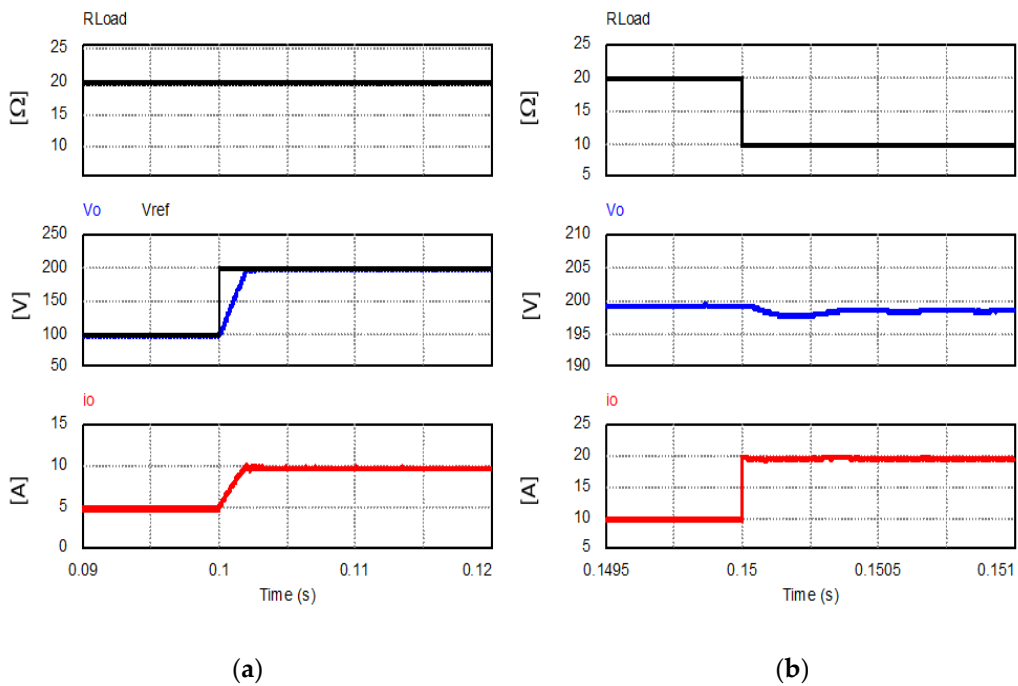


Figure 20. Simulation results with the SA. (a) Change in voltage reference, (b) sudden load change.

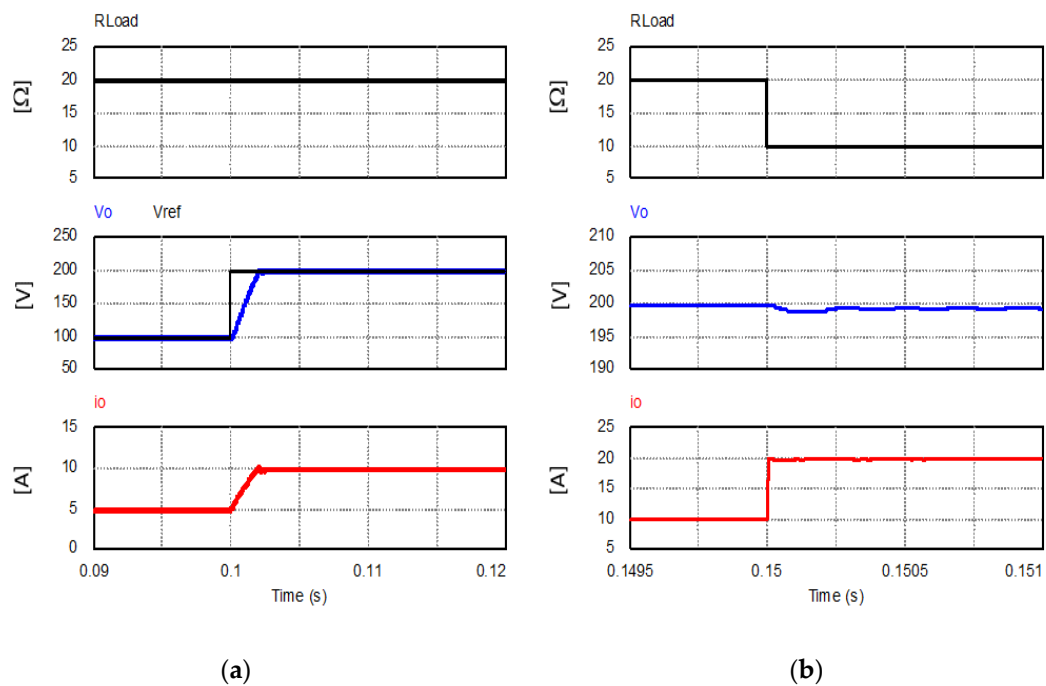


Figure 21. Simulation results with the GA. (a) Change in voltage reference, (b) sudden load change.

Secondly, the microgrid is subjected to a sudden load change, where the load resistance is increased from 20 Ω to 10 Ω. Meanwhile, the DC bus voltage reference is kept fixed to 200 V. The load disturbance occurs at $t = 0.15$ s as shown in Figures 19b, 20b and 21b for PSO, SA and GA, respectively.

The voltages displayed in these figures indicate that the FO-PI controllers tuned by GA and SA algorithms provide a smoother response than those obtained by the PSO algorithm. The percentage of steady-state errors during the microgrid load change are 0.7%, 0.9%, and 1.26% with FO-controllers tuned by GA, SA, and PSO algorithms, respectively.

In addition, the voltage response obtained for the three algorithms is depicted in Figure 22, where the three evolutionary search algorithms result in a similar transient response. Moreover, the peak overshoot is less than 3% for the three algorithms. Therefore, this event cannot yet be used as a determining factor to select the best tuning strategy.

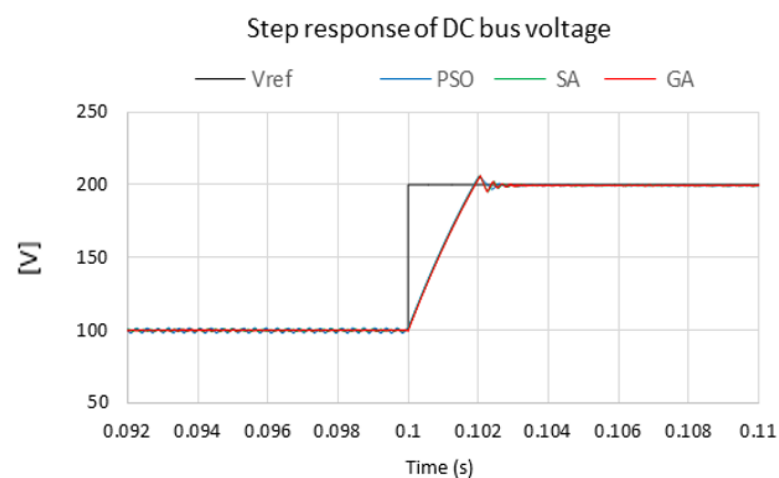


Figure 22. Comparison between the three algorithms given a step-change in voltage reference.

As shown in the comparison displayed in Figure 23, the controllers tuned by GA and SA cause a voltage dip of 3.75 V and 4.5 V, respectively. Meanwhile, the PSO leads

to a larger voltage dip, 7.5 V. Consequently, it has been demonstrated that the relatively best dynamic response is achieved with the parameters tuned by the GA in terms of voltage stability and steady-state error. In contrast, the worst response is obtained with the parameters tuned by the PSO.

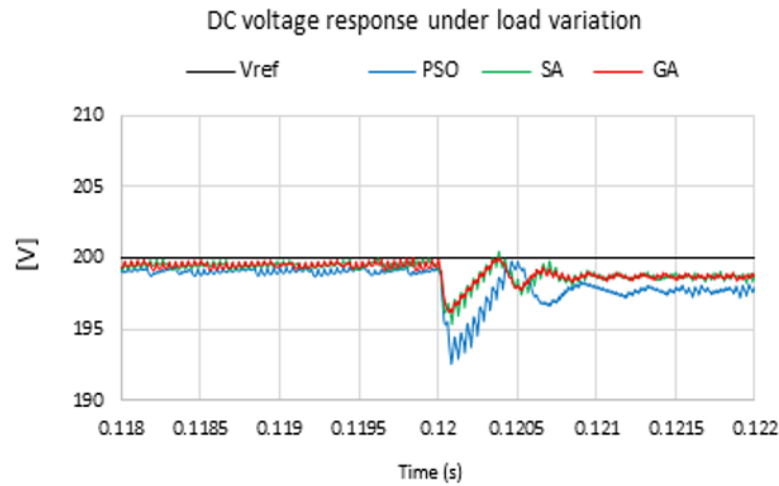
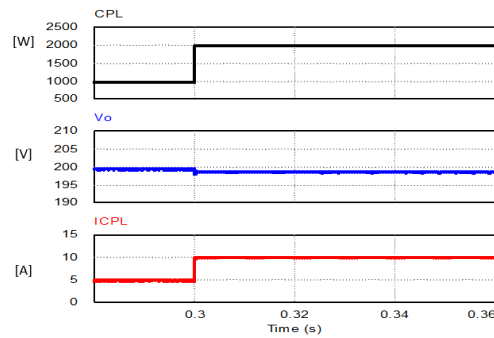


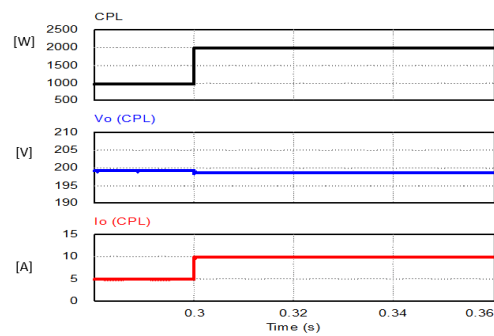
Figure 23. Voltage transient response obtained during a step-change in the load resistance.

7.4. System Response Considering a Constant Power Load

In this operating scenario, the DC microgrid is loaded with a constant power load with an initial power of 1 kW. At $t = 0.3$ s, the load power is abruptly changed to 2 kW. The corresponding system responses (i.e., the DC voltage and current) are plotted in Figure 24 for the FO-controllers tuned by PSO, SA, and GA algorithms, respectively.



(a)



(b)

Figure 24. Cont.

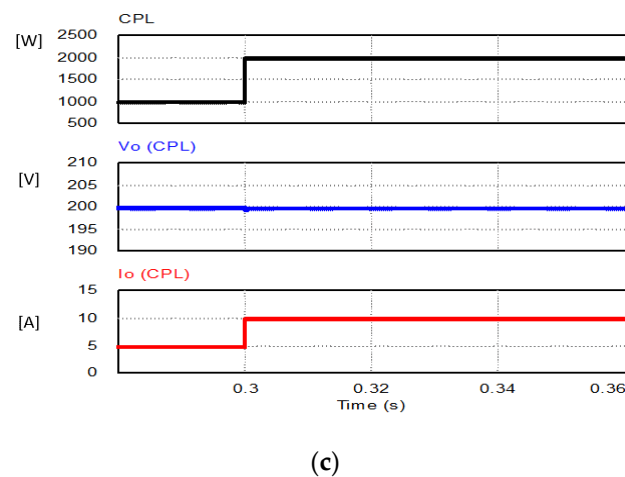


Figure 24. Simulation results for a CPL model for the three algorithms (a) PSO, (b) SA and (c) GA.

The obtained results prove that the FO controllers provide a robust response in terms of voltage stability when a constant power load increase is considered. If the FO-PI controllers tuned by PSO are analyzed, the obtained voltage drop is 1.5 V, representing a 0.75% deviation. Meanwhile, the voltage dips are 1.3 V and 0.3 V for the SA and GA, respectively. As can be observed, the FO-PI controllers tuned by the GA provide the relatively best response in terms of voltage regulation.

7.5. Response with Single-Phase Inverters

The investigated microgrid system has been tested considering AC loads feed by single-phase inverters. In practice, these inverters can be used in many applications (e.g., including pumping systems, ventilators and air conditioning systems). In this study, two operating scenarios have been presented. In the first scenario, the inverter operates in square-wave mode, producing a fixed output voltage waveform. In the second operating scenario, the inverter is working in a bipolar-SPWM mode, where the output voltage of the inverter can be controlled by adjusting the amplitude modulation index.

7.5.1. Square-Wave Single-Phase Inverter

In this subsection, the response of the DC bus voltage is illustrated with the three sets of FO-PI controller parameters. Initially, the inverter is loaded with a resistance of 60Ω , which at $t = 0.25$ s it is reduced to 20Ω . The inverter operating frequency is 60 Hz (i.e., the fundamental frequency).

The response of the microgrid has been illustrated in Figures 25–27 with the controllers' parameters tuned by PSO, SA and GA, respectively. The voltage drop during the sudden load variation proved to be 198.4 V if the controller parameters tuned by the PSO are considered, which is a deviation of 0.8% with respect to the rated DC voltage.

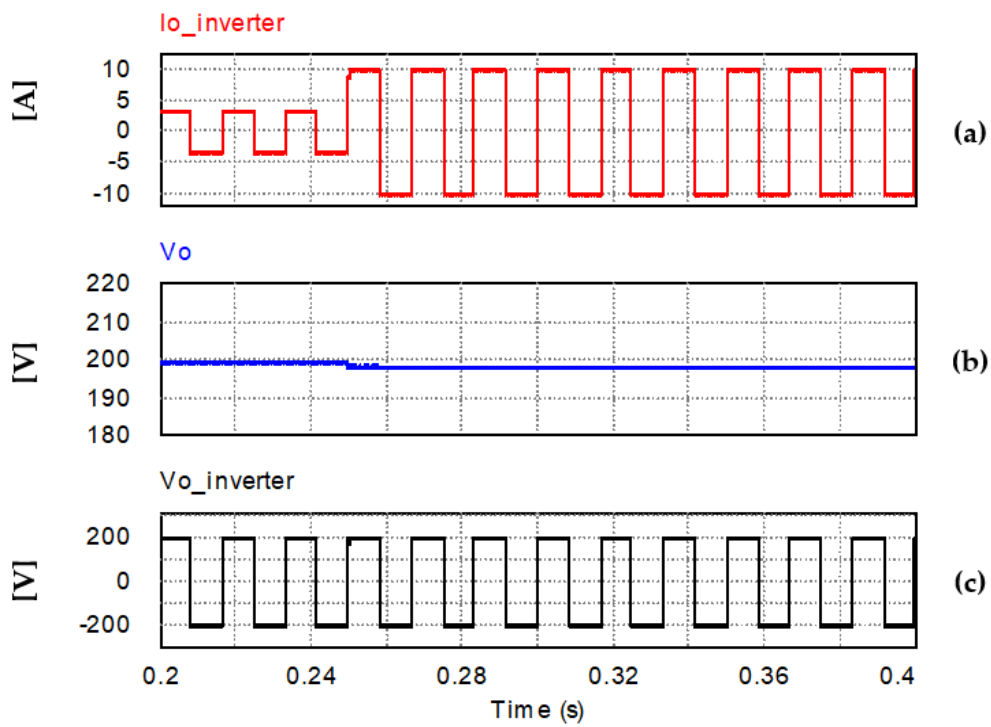


Figure 25. Microgrid response under non-linear load (square-wave inverter), (a) Inverter output current, (b) DC bus voltage, (c) Inverter output voltage in case of PSO-based tuned parameters.

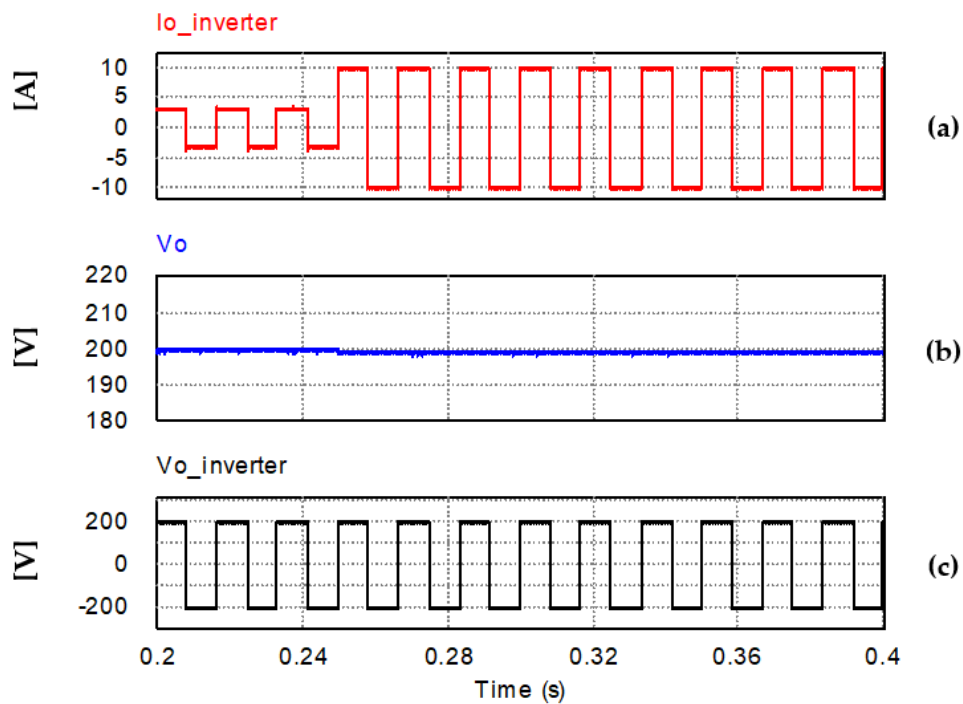


Figure 26. Microgrid response under non-linear load (square-wave inverter), (a) Inverter output current, (b) DC bus voltage, (c) Inverter output voltage in case of SA-based tuned parameters.

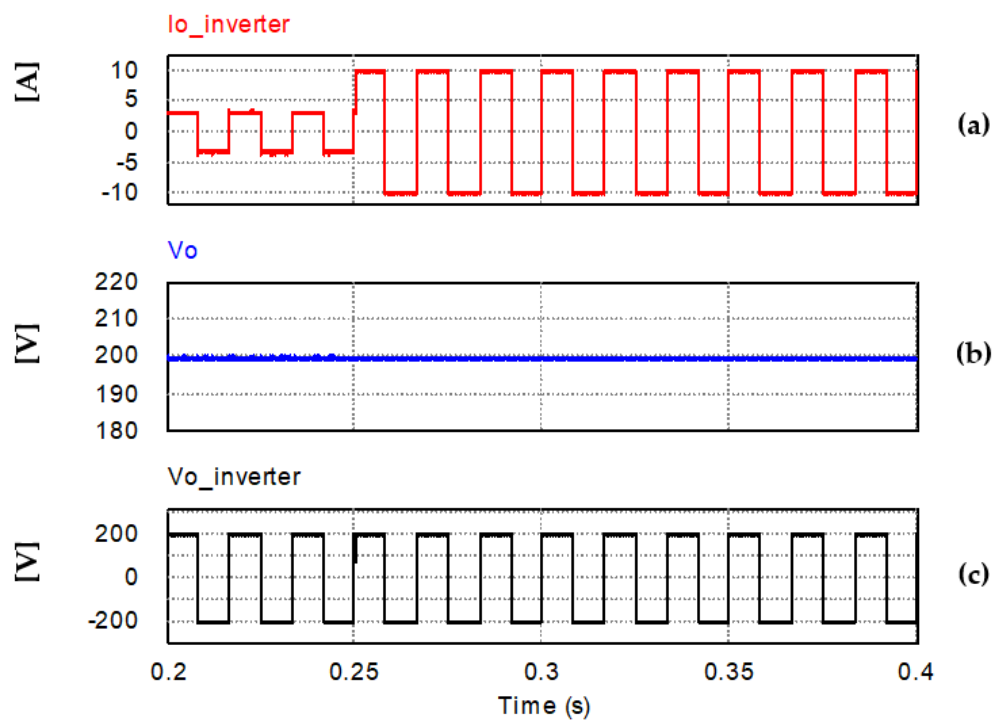


Figure 27. Microgrid response under non-linear load (square-wave inverter), (a) Inverter output current, (b) DC bus voltage, (c) Inverter output voltage in case of GA-based tuned parameters.

In Figure 25a, the inverter output current is plotted, while the resultant bus voltage is plotted in Figure 25b. The inverter output voltage is also displayed in Figure 25c.

If the SA algorithm tune the FO-PI controllers, the voltage drop caused by the load change is 198.9 V, that is, a 0.55% decrease. Figure 26a,b show the inverter current and the DC bus voltage, respectively. Moreover, the inverter voltage is illustrated in Figure 26c.

If the obtained FO-PI controller parameters obtained by the GA are considered, the bus voltage decreased to 199.7 V during the sudden load variation, representing a voltage drop of 0.15% with respect to the rated value. The inverter output current is presented in Figure 27a. On the other hand, the resultant bus voltage is plotted in Figure 27b, and the inverter output voltage is displayed in Figure 27c.

According to the obtained results, the FO-controller parameters tuned by the GA algorithm exhibit the minimum voltage drop during the load resistance change if the single-phase inverter operates in square-wave mode. In contrast, the relatively worst result has been achieved with PSO algorithm.

7.5.2. SPWM Single-Phase Inverter

The response of the DC bus voltage is illustrated in this section for the three sets of FO-PI controller parameters considering an SPWM single-phase inverter. Initially, the inverter is loaded with an RL load whose resistive and inductive values are 60 Ω and 2 mH, respectively. Afterwards, at $t = 0.25$ s, the resistive term is reduced to 20 Ω . The inverter operating frequency is 60 Hz, the switching frequency is 15 kHz and the amplitude modulation index 0.6.

The response of the microgrid has been illustrated in Figures 28–30 with controllers' parameters tuned by PSO, SA and GA, respectively.

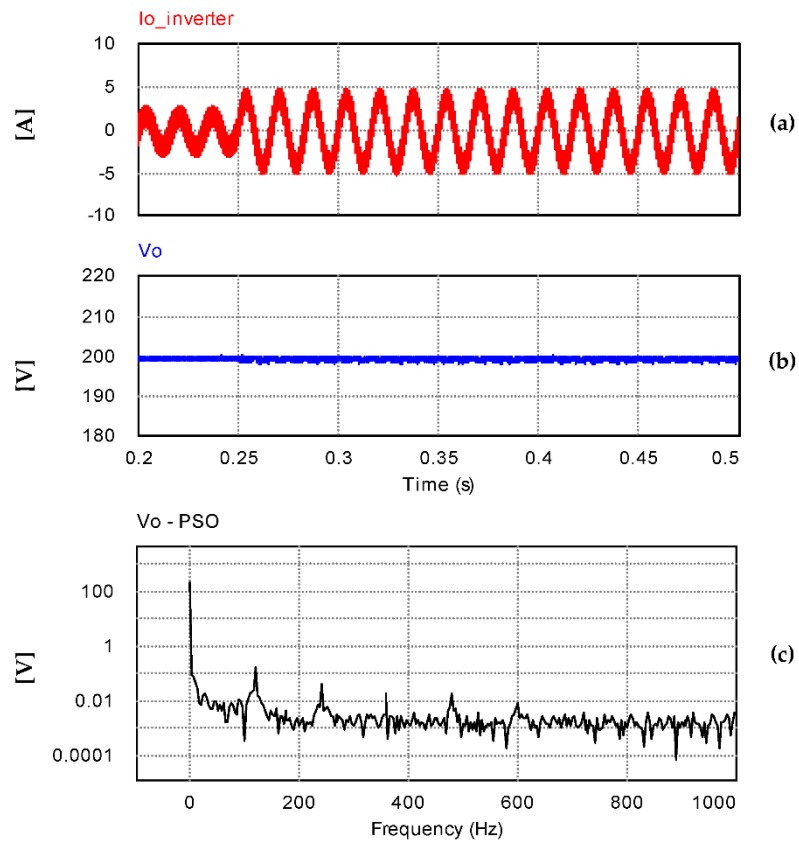


Figure 28. Microgrid response under non-linear load (SPWM inverter), (a) Inverter output current, (b) DC bus voltage, (c) Bus voltage spectral decomposition in case of PSO-based tuned parameters.

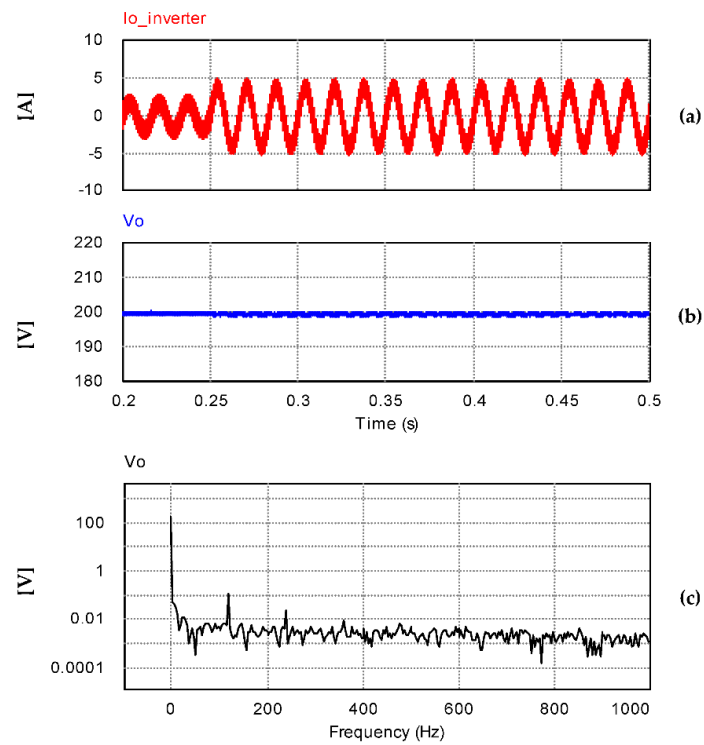


Figure 29. Microgrid response under non-linear load (SPWM inverter), (a) Inverter output current, (b) DC bus voltage, (c) Bus voltage spectral decomposition in case of SA-based tuned parameters.

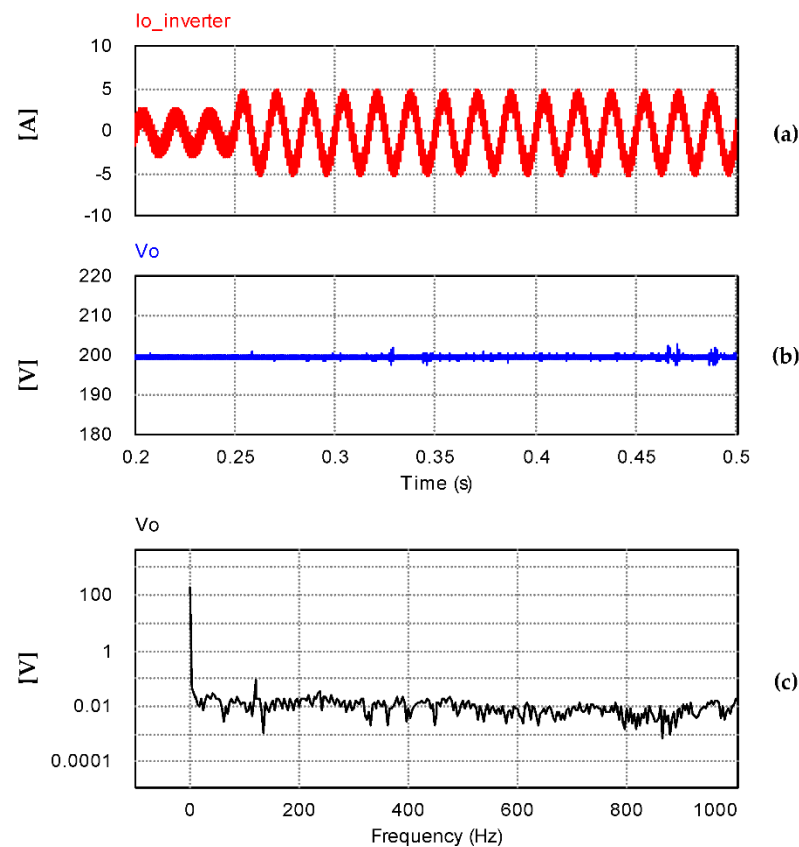


Figure 30. Microgrid response under non-linear load (SPWM inverter), (a) Inverter output current, (b) DC bus voltage, (c) Bus voltage spectral decomposition in case of GA-based tuned parameters.

During the transient caused by the sudden load connection, a negligible overvoltage has been identified with the parameters tuned by the PSO algorithm (200.3 V). Whereas, during the same event, the minimum recorded voltage value proved to be 198.6 V. The maximum peak-to-peak voltage ripple is 1.7 V, representing a 0.85% drop with respect to the rated voltage. In Figure 28a, the inverter output current is plotted, while the resultant Bus voltage is plotted in Figure 28b. In addition, the corresponding spectral decomposition of the DC bus voltage is plotted in Figure 28c. According to the obtained results of the spectral decomposition, the ripple of the DC bus voltage has a low-order harmonic content with negligible magnitudes.

When the parameters tuned by the SA are considered, a negligible overvoltage has been measured during the transient caused by the load connection, see Figure 28a. Whereas, during the same event, the minimum voltage value proved to be 199.2 V. The maximum peak-to-peak voltage ripple is 1.5 V, representing a 0.75% drop with respect to the rated voltage. Figure 29a shows that the inverter output current is plotted, while the resultant DC bus voltage is plotted in Figure 29b.

In addition, the corresponding spectral decomposition of the DC bus voltage is plotted in Figure 29c. According to the obtained results of this decomposition, it is seen that the ripple of the DC bus voltage has a low-order harmonic content with negligible magnitudes. In particular, a second-order harmonic content with a magnitude of 0.109 V is observed.

When the tuned parameters are obtained with the GA algorithm, the maximum overvoltage observed during the transient caused by the sudden load connection is 203 V (see Figure 30a). On the contrary, during the same event, the minimum voltage value proved to be 198.1 V. The maximum peak-to-peak voltage ripple is 4.9 V, representing a 2.45% drop with respect to the rated voltage.

In Figure 30a, the inverter output current is plotted, while the resultant Bus voltage is plotted in Figure 30b. In addition, the corresponding spectral decomposition of the dc bus voltage is plotted in Figure 30c.

It has been observed that if an SPWM inverter is selected to feed AC loads through the DC link, the worst achieved results in terms of peak-to-peak voltage ripple are those tuned by the GA algorithm, see the plots in Figure 30.

Considering the above, the proportional gain of the voltage controller is relatively large (i.e., K_{p1} 33.55) compared with the corresponding values achieved by the two other algorithms (i.e., K_{p1} with PSO is 9.4 and K_{p1} with SA is 16.3).

Accordingly, this gain is intentionally reduced to 30 and the response has been investigated again. The archived results of the DC bus voltage, current and, the corresponding spectral decomposition are plotted again in Figure 31a,b respectively.

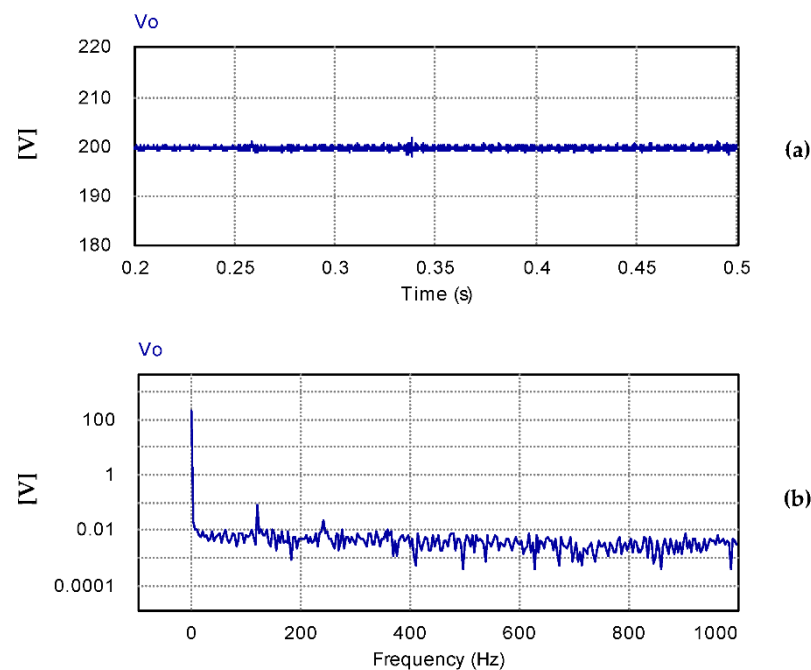


Figure 31. Microgrid response under non-linear load (SPWM inverter), in case of GA-based tuned parameters (K_{p1} is 30), (a) DC bus voltage, (b) Bus voltage spectral decomposition.

Considering this change in the value of K_{p1} , the maximum detected bus voltage is 201.7 V, while the minimum detected value is 198.4 V. Thus, the peak-to-peak voltage ripple became 3.3 V instead of 4.9 V.

According to resultant spectral decomposition, the DC bus voltage has a low order harmonic content. Thus, a slight second-order harmonic component with 0.077 V magnitude is observed.

7.6. Results of the Optimization Process

The principal comparison items in this section are the following; the convergence time of each algorithm and the steady-state value of the objective function. The evolution of fitness function has also been considered as a critical factor for comparison purposes. Accordingly, the results of the convergence are provided in Figure 32, where it is seen that all algorithms converge to the same minimum final value. However, the GA algorithm converges to the final solution after 10 iterations, the PSO algorithm after 18 iterations, while the SA algorithm's convergence is achieved in 40 iterations. The time of convergence for each algorithm is summarized in Table 6. Although the GA algorithm converges to the optimal solution with fewer iterations than the other considered algorithms, the overall convergence time is the largest when compared with the PSO and SA.

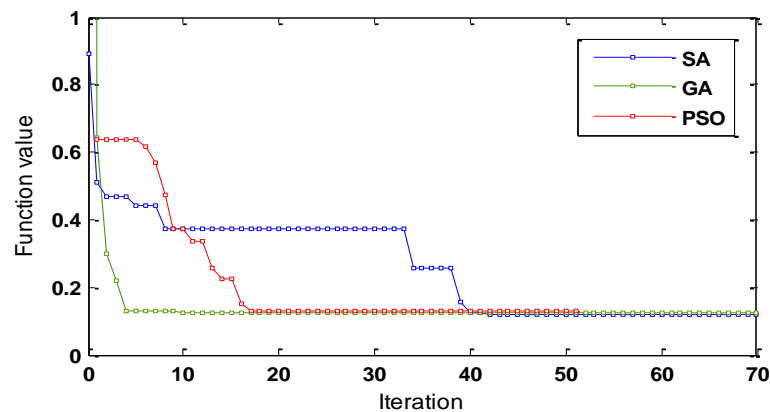


Figure 32. Evolution of the fitness function for the three algorithms.

Crucially, it has been found that SA is the fastest algorithm; meanwhile, GA is the one that takes more time for each iteration. The elapsed time for each iteration in the GA algorithm is between 10 s and 12 s, between 4 s and 6 s for the PSO and between 0.5 s and 1 s for the SA.

7.7. Impact of Parameters Uncertainty on the DC Bus Voltage

The impact of parameters variation on the DC bus voltage has been studied and summarized in this subsection. Besides load variation, four uncertain parameters have been considered in this article (leakage inductance L_k , inductor equivalent series resistance R_k , DAB input capacitance C_1 , and DAB output capacitance C_2). The impact of parameters variation is studied considering a single-phase inverter operating in square-wave mode with an AC load.

The inductance (L_k) is subjected to $\pm 30\%$ variation from the nominal value ($170 \mu\text{H}$). The resultant voltage dips under the extreme values have been listed in Table 7. The results indicate that the L_k uncertainty has a negligible effect on the DC bus voltage.

Table 7. Effect of Inductor L_k on the bus voltage.

Algorithm	Voltage Dip Due to Inductor L_k Uncertainty (L_k Nominal = $170 \mu\text{H}$)		
	$L_{k \min} = 120 \mu\text{H}$	$L_k = 170 \mu\text{H}$	$L_{k \max} = 220 \mu\text{H}$
PSO	1.60 V	1.63 V	1.70 V
SA	0.99 V	1.02 V	0.93
GA	0.50 V	0.52 V	0.51

Secondly, as shown in Table 8, two additional ESR (R_k) values have been considered (i.e., 0.05Ω and 1Ω). The resultant voltage drops with these different ESR values are summarized in Table 8. The results indicate that the R_k has a negligible effect on the DC bus voltage.

Table 8. Effect of Inductor R_k on the bus voltage.

Algorithm	Voltage Dip Due to Inductor ESR Uncertainty (R_k Nominal = 0.2Ω)		
	$R_{k \min} = 0.05 \Omega$	$R_k = 0.2 \Omega$	$R_{k \max} = 1 \Omega$
PSO	1.80 V	1.63 V	1.60 V
SA	1.05 V	1.02 V	1.02 V
GA	0.60 V	0.52 V	0.50 V

Thirdly, the DAB capacitances (C_1) and (C_2) have been subjected to a $\pm 25\%$ variation with respect to their rated value, that is, $400 \mu\text{F}$. The resultant voltage drops for these case studies are provided in Tables 9 and 10. The results indicate that both C_1 and C_2 have no noticeable effect on the DC bus voltage. The results summarized in Tables 6–10 indicate that the microgrid load is the most dominant uncertain parameter; meanwhile, as mentioned above, the other passive parameters of the DAB have negligible impact on the DC bus voltage of the microgrid.

Table 9. Effect of DAB input capacitor C_1 on the bus voltage.

Algorithm	Voltage Dip Due to Inductor L_k Uncertainty (C_1 Nominal = $400 \mu\text{F}$)		
	$C_{1 \min} = 480 \mu\text{F}$	$C_1 = 400 \mu\text{F}$	$C_{1 \max} = 320 \mu\text{F}$
PSO	1.59 V	1.63 V	1.60 V
SA	1.01 V	1.02 V	1.06 V
GA	0.51 V	0.518 V	0.519 V

Table 10. Effect of DAB output capacitor C_2 on the bus voltage.

Algorithm	Voltage Dip due to Inductor L_k Uncertainty (C_2 Nominal = $400 \mu\text{F}$)		
	$C_{2 \min} = 480 \mu\text{F}$	$C_2 = 400 \mu\text{F}$	$C_{2 \max} = 320 \mu\text{F}$
PSO	1.58 V	1.63 V	1.68 V
SA	1.00 V	1.02 V	1.05 V
GA	0.498 V	0.52 V	0.541 V

8. Comparison with Other Existing Techniques

This article has analyzed three evolutionary algorithms to tune the FO-PI controllers of a DAB for voltage stability purposes in a DC microgrid. The following comparison highlights the contribution of our assessment:

- In the available literature, several recent articles have used evolutionary algorithms to obtain optimal parameters in many applications, see [42–48]. However, any of them has been used to tune FO-PI controllers for voltage stability purposes in DC microgrids. Moreover, most of them have only used one algorithm. On the contrary, in the present paper, a comparison between three different algorithms is provided.
- Although the recently published articles towards voltage stability in DC microgrids have considered innovative approaches to address several drawbacks, they have assumed the controller parameters a fixed value without considering the optimal tuning process. For instance, see [24–29].

Lastly, it is worth mentioning that the proposed assessment has provided a robust response for voltage stability through optimal FO-PI controller parameters, enhancing the current status within this field.

9. Conclusions

In this paper, three evolutionary optimization algorithms have been used to tune the FO-PI controllers implemented in a DAB-based DC microgrid. The aim is to find the optimal parameters for these controllers in terms of voltage stability.

Firstly, the DAB small-signal model has been used for the offline optimization process. Once the three sets of optimal parameters are obtained, a frequency-domain analysis model has been developed to predict the voltage stability of the DC microgrid using the passivity-based criterion.

It has been observed that the microgrid controllers with the obtained three sets of parameters for each algorithm meet the Nyquist criterion, and therefore, stable responses

are expected. However, as seen in Section 6, the most stable scenario occurs with the parameters tuned with the GA and the less stable with the PSO algorithm.

To verify such analysis, the detailed model of the DC microgrid has been implemented in PSIM software, where the time-domain simulations are performed. These simulations have been carried out considering several test cases, including changes in the voltage reference and sudden load changes. Hence, as shown in Figure 23 of Section 7, the best dynamic response is achieved by the GA, whereas the least one occurs with the PSO. Thereby, the dependability of the stability analysis provided in Section 7 has been demonstrated. Moreover, it has also been found that the GA provides the lowest voltage ripple during the tested events.

In terms of computation, the GA algorithm is the one that takes more time for each iteration to converge, but the final overall time convergence is roughly 1.5 min, which is between SA and PSO.

By observing the features comparison contained in Table 6, it can be concluded that the GA is the algorithm that offers the best performance for voltage stability as well as an acceptable computation time.

Finally, the influence of the passive parameters of the DAB has also been analyzed. The results summarized in Tables 6–10 indicate that elements such as the DAB leakage inductor or DC link capacitances have no noticeable impact on the DC bus voltage. Therefore, it has been demonstrated that both the microgrid load model and its composition are the dominant parameters in the voltage stability assessment.

Author Contributions: Conceptualization, M.A.; methodology, M.A. and A.S.-F.; software, M.A.; formal analysis, M.A.; investigation, M.A. and A.S.-F.; stability assessment, A.S.-F.; writing—original draft preparation, M.A.; writing and editing, M.A. and A.S.-F.; revision on first draft M.A. and S.A; final revisions M.A.; A.S.-F. All authors have read and agreed to the published version of the manuscript.

Funding: This research did not receive any external funding.

Conflicts of Interest: The authors declare no conflict of interest.

Abbreviations

CPL	Constant power load
DAB	Dual Active Bridge
DC	Direct Current
ESR	Equivalent series resistance of inductor L_k
FO	Fractional Order
GA	Genetic Algorithm
HFL	High Frequency Link
PSO	Particle Swarm Optimization
SA	Simulated Annealing
SPSM	Single Phase Shift Modulation
PF	Power Factor
PID	Proportional Integral Derivative Controller
PI	Proportional Integral Controller
PV	Photovoltaic
VSI	Voltage Source Inverter
1- ϕ	Single Phase
TPS	Triple Phase Shift

Nomenclatures

L_k	Leakage inductance of inductor
R_k	ESR of inductor L_k
K_p	Proportional gain of conventional PID controller
K_i	Integral gain of conventional PID controller
K_d	Differentiator gain of conventional PID controller
$e(t)$	Error signal between reference and actual signals
$u(t)$	Output of PID controller
K_{p1}	Gain of proportional term of FO-voltage controller
K_{i1}	Gain of integral term of FO-voltage controller
λ_1	Order of integral term of FO-voltage controller
K_{p2}	Gain of proportional term of FO-current controller
K_{i2}	Gain of integral term of FO-current controller
λ_2	Order of integral term of FO-current controller
ϕ	Phase shift
d	Phase shift ratio
P_o	Average output power of DAB converter
f_s	Inverter switching frequency
G_{pid}	Transfer function of conventional PID controller
G_{foc}	Transfer function of fractional order controller
T	Temperature parameter of SA algorithm
V_{DC}	DC bus voltage
v_p	Primary voltage of HF transformer
v_s	Secondary voltage of HF transformer
n	Turns ratio of HF Transformer
J	Objective function of evolutionary algorithm
J_{PSO}	Objective function of PSO algorithm
J_{SA}	Objective function of SA algorithm
J_{GA}	Objective function of GA algorithm
w	Inertia weight of PSO algorithm
α, β	random numbers
k	Iteration number k of the PSO algorithm
i	Particle number i of the PSO algorithm
G	Global best position found by all particles
L	Local (Particle) best position
L_S	Inductance of the AC link inductor
R_S	Equivalent resistance of the AC link inductor
v_i^k	Velocity of the particle i at iteration k
n, c	Neighborhood and current solutions in SA

Appendix A

Table A1. Specifications and simulation parameters of the investigated system.

Parameter	Value
PC capability	
Processor	Intel core i3 CPU 1.7 GHz
Ram	8 GB
Simulation Platform	Matlab R2014a PSIM [®] Professional version 9.0.3
AC Grid	3-Phase AC Grid
Grid line voltage	380 V/50 HZ
DC impedance	$R_{DC} = 0.35 \Omega$ and $L_{DC} = 6 \text{ mH}$
DAB Inductor	
Leakage inductor (L_k)	170 μH
ESR of L_k (R_k)	0.2 Ω
HFL Transformer	
Turns ratio	2:1 (step down)
DC Bus	
Rated Voltage	200 V
Inverter Power Device	
Type	IGBT Branch Module
Rating	1200 V/75 A
Filter Capacitors	
Input Capacitor C_1	400 μF
Output Capacitor C_2	400 μF
Simulation sampling time	10 μs
DAB switching frequency	25 kHz

References

- Hou, N.; Li, Y.W. Overview and Comparison of Modulation and Control Strategies for a Nonresonant Single-Phase Dual-Active-Bridge DC–DC Converter. *IEEE Trans. Power Electron.* **2020**, *35*, 3148–3172. [[CrossRef](#)]
- Sun, X.; Wang, H.; Qi, L.; Liu, F. Research on Single-Stage High-Frequency-Link SST Topology and Its Optimization Control. *IEEE Trans. Power Electron.* **2020**, *35*, 8701–8711. [[CrossRef](#)]
- Xia, P.; Shi, H.; Wen, H.; Bu, Q.; Hu, Y.; Yang, Y. Robust LMI-LQR Control for Dual-Active-Bridge DC–DC Converters with High Parameter Uncertainties. *IEEE Trans. Transp. Electr.* **2020**, *6*, 131–145. [[CrossRef](#)]
- Liu, P.; Duan, S. A Hybrid Modulation Strategy Providing Lower Inductor Current for the DAB Converter with the Aid of DC Blocking Capacitors. *IEEE Trans. Power Electron.* **2019**, *35*, 4309–4320. [[CrossRef](#)]
- Hou, N.; Song, W.; Li, Y.W.; Zhu, Y.; Zhu, Y. A Comprehensive Optimization Control of Dual-Active-Bridge DC–DC Converters Based on Unified-Phase-Shift and Power-Balancing Scheme. *IEEE Trans. Power Electron.* **2018**, *34*, 826–839. [[CrossRef](#)]
- Hebala, O.M.; Aboushady, A.A.; Ahmed, K.H.; Abdelsalam, I.A. Generic Closed-Loop Controller for Power Regulation in Dual Active Bridge DC–DC Converter with Current Stress Minimization. *IEEE Trans. Ind. Electron.* **2019**, *66*, 4468–4478. [[CrossRef](#)]
- Liu, Y.; Wang, X.; Qian, W.; Janabi, A.; Wang, B.; Lu, X.; Zou, K.; Chen, C.; Peng, F.Z. A Simple Phase-Shift Modulation Using Parabolic Carrier for Dual Active Bridge DC–DC Converter. *IEEE Trans. Power Electron.* **2020**, *35*, 7729–7734. [[CrossRef](#)]
- Voss, J.; Engel, S.P.; De Doncker, R.W. Control Method for Avoiding Transformer Saturation in High-Power Three-Phase Dual-Active Bridge DC–DC Converters. *IEEE Trans. Power Electron.* **2020**, *35*, 4332–4341. [[CrossRef](#)]
- Kwak, B.; Kim, M.; Kim, J. Inrush current reduction technology of DAB converter for low-voltage battery systems and DC bus connections in DC microgrids. *IET Power Electron.* **2020**, *13*, 1528–1536. [[CrossRef](#)]
- Chen, L.; Shao, S.; Xiao, Q.; Tarisciotti, L.; Wheeler, P.W.; Dragicevic, T. Model Predictive Control for Dual-Active-Bridge Converters Supplying Pulsed Power Loads in Naval DC Micro-Grids. *IEEE Trans. Power Electron.* **2020**, *35*, 1957–1966. [[CrossRef](#)]
- An, F.; Song, W.; Yu, B.; Yang, K. Model Predictive Control with Power Self-Balancing of the Output Parallel DAB DC–DC Converters in Power Electronic Traction Transformer. *IEEE J. Emerg. Sel. Top. Power Electron.* **2018**, *6*, 1806–1818. [[CrossRef](#)]
- An, F.; Song, W.; Yang, K. Direct power control of dual-active-bridge dc–dc converters based on unified phase shift control. *J. Eng.* **2019**, *2019*, 2180–2184. [[CrossRef](#)]

13. Song, W.; Hou, N.; Wu, M. Virtual Direct Power Control Scheme of Dual Active Bridge DC–DC Converters for Fast Dynamic Response. *IEEE Trans. Power Electron.* **2018**, *33*, 1750–1759. [[CrossRef](#)]
14. Shan, Z.; Jatskevich, J.; Iu, H.H.-C.; Fernando, T. Simplified Load-Feedforward Control Design for Dual-Active-Bridge Converters with Current-Mode Modulation. *IEEE J. Emerg. Sel. Top. Power Electron.* **2018**, *6*, 2073–2085. [[CrossRef](#)]
15. Wang, D.; Nahid-Mobarakeh, B.; Emadi, A. Second Harmonic Current Reduction for a Battery-Driven Grid Interface with Three-Phase Dual Active Bridge DC–DC Converter. *IEEE Trans. Ind. Electron.* **2019**, *66*, 9056–9064. [[CrossRef](#)]
16. Zengin, S.; Boztepe, M. A Novel Current Modulation Method to Eliminate Low-Frequency Harmonics in Single-Stage Dual Active Bridge AC–DC Converter. *IEEE Trans. Ind. Electron.* **2020**, *67*, 1048–1058. [[CrossRef](#)]
17. Datta, A.J.; Ghosh, A.; Zare, F.; Rajakaruna, S. Bidirectional power sharing in an ac/dc system with a dual active bridge converter. *IET Gener. Transm. Distrib.* **2019**, *13*, 495–501. [[CrossRef](#)]
18. Shao, S.; Jiang, M.; Ye, W.; Li, Y.; Zhang, J.; Sheng, K. Optimal Phase-Shift Control to Minimize Reactive Power for a Dual Active Bridge DC–DC Converter. *IEEE Trans. Power Electron.* **2019**, *34*, 10193–10205. [[CrossRef](#)]
19. Wu, J.; Wen, P.; Sun, X.; Yan, X. Reactive Power Optimization Control for Bidirectional Dual-Tank Resonant DC–DC Converters for Fuel Cells Systems. *IEEE Trans. Power Electron.* **2020**, *35*, 9202–9214. [[CrossRef](#)]
20. Gu, Q.; Yuan, L.; Nie, J.; Sun, J.; Zhao, Z. Current Stress Minimization of Dual-Active-Bridge DC–DC Converter Within the Whole Operating Range. *IEEE J. Emerg. Sel. Top. Power Electron.* **2019**, *7*, 129–142. [[CrossRef](#)]
21. Vuyyuru, U.; Maiti, S.; Chakraborty, C. Active Power Flow Control between DC Microgrids. *IEEE Trans. Smart Grid* **2019**, *10*, 5712–5723. [[CrossRef](#)]
22. Jeung, Y.C.; Lee, D.C. Voltage and Current Regulations of Bidirectional Isolated Dual-Active-Bridge DC–DC Converters Based on a Double-Integral Sliding Mode Control. *IEEE Trans. Power Electron.* **2019**, *34*, 6937–6946. [[CrossRef](#)]
23. You, J.; Vilathgamuwa, M.; Ghasemi, N. DC bus voltage stability improvement using disturbance observer feedforward control. *Control. Eng. Pr.* **2018**, *75*, 118–125. [[CrossRef](#)]
24. Jeung, Y.C.; Lee, D.C.; Dragicevic, T.; Blaabjerg, F. Design of Passivity-Based Damping Controller for Suppressing Power Oscillations in DC Microgrids. *IEEE Trans. Power Electron.* **2021**, *36*, 4016–4028. [[CrossRef](#)]
25. Li, X.; Guo, L.; Zhang, S.; Wang, C.; Li, Y.W.; Chen, A.; Feng, Y. Observer-Based DC Voltage Droop and Current Feed-Forward Control of a DC Microgrid. *IEEE Trans. Smart Grid* **2018**, *9*, 5207–5216. [[CrossRef](#)]
26. Chen, L.; Gao, F.; Shen, K.; Wang, Z.; Tarisciotti, L.; Wheeler, P.; Dragicevic, T. Predictive Control Based DC Microgrid Stabilization with the Dual Active Bridge Converter. *IEEE Trans. Ind. Electron.* **2020**, *67*, 8944–8956. [[CrossRef](#)]
27. Ye, Q.; Mo, R.; Li, H. Impedance Modeling and DC Bus Voltage Stability Assessment of a Solid-State-Transformer-Enabled Hybrid AC–DC Grid Considering Bidirectional Power Flow. *IEEE Trans. Ind. Electron.* **2019**, *67*, 6531–6540. [[CrossRef](#)]
28. Bosich, D.; Vicenzutti, A.; Grillo, S.; Sulligoi, G. A Stability Preserving Criterion for the Management of DC Microgrids Supplied by a Floating Bus. *Appl. Sci.* **2018**, *8*, 2102. [[CrossRef](#)]
29. Feng, F.; Zhang, X.; Zhang, J.; Gooi, H.B. Stability Enhancement via Controller Optimization and Impedance Shaping for Dual Active Bridge-Based Energy Storage Systems. *IEEE Trans. Ind. Electron.* **2020**, *68*, 5863–5874. [[CrossRef](#)]
30. Dragicevic, T.; Lu, X.; Vasquez, J.C.; Guerrero, J.M. DC Microgrids—Part I: A Review of Control Strategies and Stabilization Techniques. *IEEE Trans. Power Electron.* **2015**, *31*, 4876–4891. [[CrossRef](#)]
31. Rodriguez, A.; Vazquez, A.; Lamar, D.G.; Hernando, M.M.; Sebastian, J. Different Purpose Design Strategies and Techniques to Improve the Performance of a Dual Active Bridge with Phase-Shift Control. *IEEE Trans. Power Electron.* **2015**, *30*, 790–804. [[CrossRef](#)]
32. Liu, L.; Shan, L.; Dai, Y.; Liu, C.; Qi, Z. Improved quantum bacterial foraging algorithm for tuning parameters of fractional-order PID controller. *J. Syst. Eng. Electron.* **2018**, *29*, 166–175. [[CrossRef](#)]
33. Meng, F.; Liu, S.; Liu, K. Design of an Optimal Fractional Order PID for Constant Tension Control System. *IEEE Access* **2020**, *8*, 58933–58939. [[CrossRef](#)]
34. Yaghi, M.A.; Efe, M.O. H₂/H_∞H₂/H_∞-Neural-Based FOPID Controller Applied for Radar-Guided Missile. *IEEE Trans. Ind. Electron.* **2019**, *67*, 4806–4814. [[CrossRef](#)]
35. Chen, C.L. Simulated annealing-based optimal wind-thermal coordination scheduling. *IET Gener. Transm. Distrib.* **2007**, *1*, 447. [[CrossRef](#)]
36. Ricobono, A.; Santi, E. Positive feedforward control of three-phase voltage source inverter for DC input bus stabilization with experimental validation. *IEEE Trans. Ind. Appl.* **2013**, *49*, 168–177. [[CrossRef](#)]
37. Shi, H.; Sun, K.; Wu, H.; Li, Y. A Unified State-Space Modeling Method for a Phase-Shift Controlled Bidirectional Dual-Active Half-Bridge Converter. *IEEE Trans. Power Electron.* **2019**, *35*, 3254–3265. [[CrossRef](#)]
38. Berger, M.; Kocar, I.; Fortin-Blanchette, H.; Lavertu, C. Large-signal modeling of three-phase dual active bridge converters for electromagnetic transient analysis in DC grids. *J. Mod. Power Syst. Clean Energy* **2019**, *7*, 1684–1696. [[CrossRef](#)]
39. Shah, S.S.; Bhattacharya, S. A Simple Unified Model for Generic Operation of Dual Active Bridge Converter. *IEEE Trans. Ind. Electron.* **2019**, *66*, 3486–3495. [[CrossRef](#)]
40. Cupelli, M.; Gurumurthy, S.K.; Bhandari, S.K.; Yang, Z.; Joebges, P.; Monti, A.; De Doncker, R.W. Port Controlled Hamiltonian Modeling and IDA-PBC Control of Dual Active Bridge Converters for DC Microgrids. *IEEE Trans. Ind. Electron.* **2019**, *66*, 9065–9075. [[CrossRef](#)]

41. Birs, I.; Muresan, C.; Nascu, I.; Ionescu, C. A Survey of Recent Advances in Fractional Order Control for Time Delay Systems. *IEEE Access* **2019**, *7*, 30951–30965. [[CrossRef](#)]
42. Pullaguram, D.; Mishra, S.; Senroy, N.; Mukherjee, M. Design and Tuning of Robust Fractional Order Controller for Autonomous Microgrid VSC System. *IEEE Trans. Ind. Appl.* **2017**, *54*, 91–101. [[CrossRef](#)]
43. Tolba, M.F.; Said, L.A.; Madian, A.H.; Radwan, A.G. FPGA Implementation of the Fractional Order Integrator/Differentiator: Two Approaches and Applications. *IEEE Trans. Circuits Syst. I Regul. Pap.* **2018**, *66*, 1484–1495. [[CrossRef](#)]
44. Seo, S.-W.; Choi, H.H. Digital Implementation of Fractional Order PID-Type Controller for Boost DC–DC Converter. *IEEE Access* **2019**, *7*, 142652–142662. [[CrossRef](#)]
45. Liu, L.; Zhang, S.; Xue, D.; Chen, Y.Q. General robustness analysis and robust fractional-order PD controller design for fractional-order plants. *IET Control. Theory Appl.* **2018**, *12*, 1730–1736. [[CrossRef](#)]
46. Ren, H.P.; Fan, J.T.; Kaynak, O. Optimal Design of a Fractional-Order Proportional-Integer-Differential Controller for a Pneumatic Position Servo System. *IEEE Trans. Ind. Electron.* **2018**, *66*, 6220–6229. [[CrossRef](#)]
47. Lino, P.; Maione, G.; Stasi, S.; Padula, F.; Visioli, A. Synthesis of fractional-order PI controllers and fractional-order filters for industrial electrical drives. *IEEE/CAA J. Autom. Sin.* **2017**, *4*, 58–69. [[CrossRef](#)]
48. Zaihidee, F.M.; Mekhilef, S.; Mubin, M. Application of Fractional Order Sliding Mode Control for Speed Control of Permanent Magnet Synchronous Motor. *IEEE Access* **2019**, *7*, 101765–101774. [[CrossRef](#)]
49. Maddahi, A.; Sepehri, N.; Kinsner, W. Fractional-Order Control of Hydraulically Powered Actuators: Controller Design and Experimental Validation. *IEEE/ASME Trans. Mechatron.* **2019**, *24*, 796–807. [[CrossRef](#)]
50. Crespo, T.; Duarte, M.A.; Ceballos, G.; Lefranc, G. Fractional Order Controllers for Back-to-Back Converters. *IEEE Lat. Am. Trans.* **2018**, *16*, 2427–2434. [[CrossRef](#)]
51. Wan, J.; He, B.; Wang, D.; Yan, T.; Shen, Y. Fractional-Order PID Motion Control for AUV Using Cloud-Model-Based Quantum Genetic Algorithm. *IEEE Access* **2019**, *7*, 124828–124843. [[CrossRef](#)]
52. Sathishkumar, P.; Selvagesan, N. Fractional Controller Tuning Expressions for a Universal Plant Structure. *IEEE Control. Syst. Lett.* **2018**, *2*, 345–350. [[CrossRef](#)]
53. Hekimoglu, B. Optimal Tuning of Fractional Order PID Controller for DC Motor Speed Control via Chaotic Atom Search Optimization Algorithm. *IEEE Access* **2019**, *7*, 38100–38114. [[CrossRef](#)]
54. Mishra, A.K.; Das, S.R.; Ray, P.K.; Mallick, R.K.; Mohanty, A.; Mishra, D.K. PSO-GWO Optimized Fractional Order PID Based Hybrid Shunt Active Power Filter for Power Quality Improvements. *IEEE Access* **2020**, *8*, 74497–74512. [[CrossRef](#)]
55. Lyden, S.; Haque, E. A Simulated Annealing Global Maximum Power Point Tracking Approach for PV Modules Under Partial Shading Conditions. *IEEE Trans. Power Electron.* **2016**, *31*, 4171–4181. [[CrossRef](#)]
56. Delahaye, D.; Chaimatanan, S.; Mongeau, M. Simulated Annealing: From Basics to Applications. In *Handbook of Metaheuristics*; Gendreau, M., Potvin, J.Y., Eds.; Springer: Berlin/Heidelberg, Germany, 2019.
57. Corus, D.; Oliveto, P.S. Standard Steady State Genetic Algorithms Can Hillclimb Faster Than Mutation-Only Evolutionary Algorithms. *IEEE Trans. Evol. Comput.* **2017**, *22*, 720–732. [[CrossRef](#)]
58. Wang, Z.; Li, J.; Fan, K.; Ma, W.; Lei, H. Prediction Method for Low Speed Characteristics of Compressor Based on Modified Similarity Theory with Genetic Algorithm. *IEEE Access* **2018**, *6*, 36834–36839. [[CrossRef](#)]
59. Mohammadi, A.; Asadi, H.; Mohamed, S.; Nelson, K.; Nahavandi, S. Multiobjective and Interactive Genetic Algorithms for Weight Tuning of a Model Predictive Control-Based Motion Cueing Algorithm. *IEEE Trans. Cybern.* **2019**, *49*, 3471–3481. [[CrossRef](#)] [[PubMed](#)]
60. Han, C.; Wang, L.; Zhang, Z.; Xie, J.; Xing, Z. A Multi-Objective Genetic Algorithm Based on Fitting and Interpolation. *IEEE Access* **2018**, *6*, 22920–22929. [[CrossRef](#)]
61. Yang, H.; Qi, J.; Miao, Y.; Sun, H.; Li, J. A New Robot Navigation Algorithm Based on a Double-Layer Ant Algorithm and Trajectory Optimization. *IEEE Trans. Ind. Electron.* **2018**, *66*, 8557–8566. [[CrossRef](#)]
62. Ma, Y.N.; Gong, Y.J.; Xiao, C.F.; Gao, Y.; Zhang, J. Path Planning for Autonomous Underwater Vehicles: An Ant Colony Algorithm Incorporating Alarm Pheromone. *IEEE Trans. Veh. Technol.* **2019**, *68*, 141–154. [[CrossRef](#)]
63. Zhang, Y.H.; Gong, Y.; Chen, W.N.; Gu, T.L.; Yuan, H.Q.; Zhang, J. A Dual-Colony Ant Algorithm for the Receiving and Shipping Door Assignments in Cross-Docks. *IEEE Trans. Intell. Transp. Syst.* **2018**, *20*, 2523–2539. [[CrossRef](#)]
64. Lee, J.H.; Song, J.Y.; Kim, D.W.; Kim, J.W.; Kim, Y.J.; Jung, S.Y. Particle Swarm Optimization Algorithm with Intelligent Particle Number Control for Optimal Design of Electric Machines. *IEEE Trans. Ind. Electron.* **2018**, *65*, 1791–1798. [[CrossRef](#)]
65. Azab, M. Multi-objective design approach of passive filters for single-phase distributed energy grid integration systems using particle swarm optimization. *Energy Rep.* **2020**, *6*, 157–172. [[CrossRef](#)]
66. Liu, Z.H.; Wei, H.L.; Zhong, Q.C.; Liu, K.; Xiao, X.S.; Wu, L.H. Parameter Estimation for VSI-Fed PMSM Based on a Dynamic PSO With Learning Strategies. *IEEE Trans. Power Electron.* **2016**, *32*, 3154–3165. [[CrossRef](#)]
67. Azab, M. Design approach and performance analysis of trap filter for three-phase PV grid integration systems using evolutionary search algorithms. *J. King Saud Univ. Eng. Sci.* **2020**. [[CrossRef](#)]
68. Sebthamadi, S.S.; Azad, H.B.; Kaboli, S.H.A.; Islam, D.; Mekhilef, S. A PSO-DQ Current Control Scheme for Performance Enhancement of Z-Source Matrix Converter to Drive IM Fed by Abnormal Voltage. *IEEE Trans. Power Electron.* **2017**, *33*, 1666–1681. [[CrossRef](#)]

69. Sarker, K.; Chatterjee, D.; Goswami, S.K. Modified harmonic minimisation technique for doubly fed induction generators with solar-wind hybrid system using biogeography-based optimisation. *IET Power Electron.* **2018**, *11*, 1640–1651. [[CrossRef](#)]
70. Pietilainen, K.; Harnefors, L.; Petersson, A.; Nee, H.P. DC-Link Stabilization and Voltage Sag Ride-Through of Inverter Drives. *IEEE Trans. Ind. Electron.* **2006**, *53*, 1261–1268. [[CrossRef](#)]
71. Mueller, J.A.; Kimball, J.W. Modeling Dual Active Bridge Converters in DC Distribution Systems. *IEEE Trans. Power Electron.* **2018**, *34*, 5867–5879. [[CrossRef](#)]
72. Tian, Y.; Peng, F.; Wang, Y.; Chen, Z. Coordinative impedance damping control for back-to-back converter in solar power integration system. *IET Renew. Power Gener.* **2019**, *13*, 1484–1492. [[CrossRef](#)]
73. Zhao, N.; Liu, J.; Ai, Y.; Yang, J.; Zhang, J.; You, X. Power-Linked Predictive Control Strategy for Power Electronic Traction Transformer. *IEEE Trans. Power Electron.* **2020**, *35*, 6559–6571. [[CrossRef](#)]
74. Chen, L.; Lin, L.; Shao, S.; Gao, F.; Wang, Z.; Wheeler, P.W.; Dragicevic, T. Moving Discretized Control Set Model-Predictive Control for Dual-Active Bridge with the Triple-Phase Shift. *IEEE Trans. Power Electron.* **2020**, *35*, 8624–8637. [[CrossRef](#)]